*J. Fluid Mech.* (2022), *vol*. 947, A38, doi:10.1017/jfm.2022.660

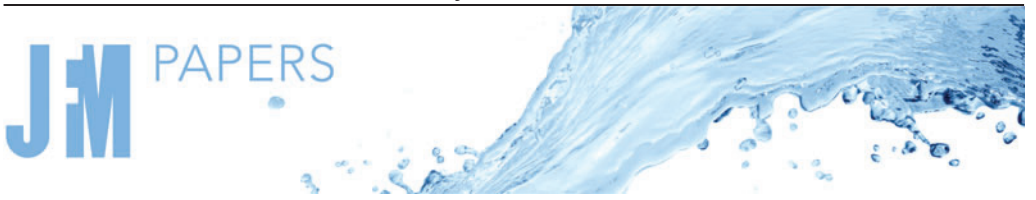

# Compressibility effects on statistics and coherent structures of compressible turbulent mixing layers

**Xiaoning Wang**[1,2,3], **Jianchun Wang**[1,2,3,†] **and Shiyi Chen**[1,2,3]

[1]Department of Mechanics and Aerospace Engineering, Southern University of Science and Technology, Shenzhen 518055, PR China

[2]Southern Marine Science and Engineering Guangdong Laboratory, Guangzhou 511458, P.R. China

[3]Guangdong-Hong Kong-Macao Joint Laboratory for Data-Driven Fluid Mechanics and Engineering Applications, Southern University of Science and Technology, Shenzhen 518055, PR China

(Received 10 April 2022; revised 11 July 2022; accepted 22 July 2022)

The effects of compressibility on the statistics and coherent structures of a temporally developing mixing layer are studied using numerical simulations at convective Mach numbers ranging from $M_c = 0.2$ to 1.8 and at Taylor Reynolds numbers up to 290. As the convective Mach number increases, the streamwise dissipation becomes more effective to suppress the turbulent kinetic energy. At $M_c = 1.8$, the streamwise dissipation increases much faster than the other two components in the transition region, even larger than pressure–strain redistribution, correlating with the streamwise elongated vortical structures at a higher level of compressibility. We confirm the existence of the large-scale high- and low-speed structures in the mixing layers, which accompany the spanwise Kelvin–Helmholtz rollers at low convective Mach number and dominate the mixing layer at higher convective Mach number. Conditional statistics demonstrate that the large-scale low-speed structures are lifted upwards by a pair of counter-rotating quasi-streamwise rollers flanking the structures. The small-scale vortical structures have an apparent preference for clustering into the top of the low-speed regions, which is directly associated with high-shearing motions on top of the low-speed structures. The high-speed structures statistically exhibit central symmetry with the low-speed structures. The statistics and dynamics of large-scale high- and low-speed structures in the compressible mixing layers resemble those in the outer region of the turbulent boundary layers, which reveals the universality of the large-scale structures in free shear and wall-bounded turbulence. A conceptual model is introduced for the large-scale high- and low-speed structures in turbulent mixing layers.

**Key words:** shear layer turbulence, turbulence simulation

† Email address for correspondence: wangjc@sustech.edu.cn

## 1. Introduction

Compressibility has a stabilising effect on a variety of high-speed shear flows, including homogeneously sheared turbulence (Sarkar 1995; Kumar, Bertsch & Girimaji 2014; Chen *et al.* 2018), turbulent mixing layers (Papamoschou & Roshko 1988; Pantano & Sarkar 2002; Arun *et al.* 2019; Li *et al.* 2021) and wall-bounded turbulence (Huang, Coleman & Bradshaw 1995; Pirozzoli & Bernardini 2011; Bross, Scharnowski & Kähler 2021; Xu *et al.* 2021*b*). The planar mixing shear layer is the simplest flow configuration of practical turbulent flow, devoid of the complexities of wall effect. However, it plays a key role in many applications, including scramjet engines, reduction of supersonic jet noise and inertial-confinement fusion (Dimotakis 1991; Lele 1994; Pope 2000).

In compressible mixing layers, the growth of the mixing shear layer is substantially reduced at high Mach numbers. An early experimental study conducted by Birch & Eggers (1972) showed that high Mach number can lead to the reduction in the growth rate of the mixing layer. Dominant spanwise rollers were observed by Brown & Roshko (1974) in compressible free shear layer with different ratios of densities across the shear layer, and they suggested that the growth rate of a turbulent free shear layer is significantly affected by compressibility rather than density ratio. Numerous studies attempted to explain the suppression mechanism of compressibility from the perspective of kinetic energy transfer (Sarkar 1995; Vreman, Sandham & Luo 1996; Pantano & Sarkar 2002; Atoufi, Fathali & Lessani 2015; Arun *et al.* 2021; Li *et al.* 2021). Sarkar (1995) performed direct numerical simulation (DNS) of compressible homogeneous shear flow, and observed a reduction in the growth rate of turbulent kinetic energy (TKE) by the increase of the gradient Mach number. He reported that the reduction of turbulent energy growth rate is primarily due to the reduced level of turbulence production and not due to explicit dilatational effects (pressure dilatation and compressible dissipation), and pressure–strain correlation tensor is significantly changed due to compressibility. Vreman *et al.* (1996) found that the dilatational contribution to dissipation is negligible even when eddy shocklets are observed in a compressible turbulent mixing layer. Furthermore, he reported that reduced pressure fluctuations are responsible for the changes in growth rate via the pressure–strain term. Pantano & Sarkar (2002) and Foysi & Sarkar (2010) confirmed that the reduced turbulence levels and mixing-layer spread rate at high Mach number are attributed to the suppression of pressure–strain redistribution. Atoufi *et al.* (2015) and Li *et al.* (2021) examined the energy exchange mechanisms in compressible turbulent mixing layer by analysing the budget terms of mean kinetic, internal and TKE transport equations. Arun *et al.* (2021) investigated the scale-space transport of TKE at different Mach numbers using DNS data of mixing layers. They showed that production is influenced by long-distance interactions, whereas the pressure dilatation effects are more localised.

There is a large volume of published studies describing the compressibility effect on coherent structures in mixing layers. In incompressible and weakly compressible mixing shear layers, the flow is dominated by large, predominantly two-dimensional, spanwise vortex structures (rollers) and rib-like vortices that arise from the Kelvin–Helmholtz instability of the layer (Rogers & Moser 1994; Balaras, Piomelli & Wallace 2001; Wang, Tanahashi & Miyauchi 2007). As the mixing layer becomes more compressible, the large roller structures break down and the vortical structures are greatly stretched in the streamwise direction, which leads to different mixing characteristics (Sandham & Reynolds 1991; Balaras *et al.* 2001; Rossmann, Mungal & Hanson 2002; Fathali *et al.* 2008; Hickey, Hussain & Wu 2016; Arun *et al.* 2019; Li *et al.* 2021). In DNSs of spatially evolving mixing layers by Zhou, He & Shen (2012), it was observed that $\Lambda$ structures in the flow field evolve to hairpin vortices which eventually break down to slender vortices

before the flow reaches a self-similar state. A recent numerical study of mixing layers by Arun *et al.* (2019) showed that the vortical structures at high Mach number tend to align in the streamwise direction but the tendency is weaker compared with that at low Mach number, which results in reduced levels of the Reynolds shear stress and suppression of turbulent energy production. They also found that the orientations of the vortex vectors are less sensitive to compressibility effects with the increase of time.

However, most of the aforementioned studies are particularly focused on the small-scale vortical structures and the spanwise Kelvin–Helmholtz vortices in mixing layers. In the experimental study of a spatially developing mixing layer, Mungal (1995) observed that the large-scale structures are elongated in the streamwise direction at moderate convective Mach numbers $M_c \approx 0.8$. The convective Mach number is defined as $M_c = \Delta U/(c_1 + c_2)$ (Bogdanoff 1983), where $c_1$ and $c_2$ are the speed of sound in the upper and lower streams and $\Delta U$ is the free-stream velocity difference across the shear layer. Messersmith & Dutton (1996) found that the size of the streamwise-oriented large structures in compressible mixing layers generally increases with increasing compressibility. DNS of the spatially developing mixing layer was carried out by Pirozzoli *et al.* (2015) at moderate compressibility conditions ($M_c \approx 0.45$). They observed that the streamwise velocity organises itself into large-scale low- and high-speed streaks, the size of which is found to grow in the streamwise and spanwise direction with an approximately proportional fashion to the local vorticity thickness. The dynamic mode decomposition (DMD) has been used to extract the spanwise rollers, which are not clearly visible in the instantaneous streamwise velocity.

The low- and high-speed large-scale coherent structures residing in the log-law layer of wall-bounded shear flow have been extensively studied in the last two decades (Ganapathisubramani *et al.* 2005; Marusic, Mathis & Hutchins 2010; Smits, McKeon & Marusic 2011; Jiménez 2018), and they have been shown to carry significant fraction of TKE and Reynolds shear stress, and interact evidently with the small-scale structures near the wall. Bross *et al.* (2021) experimentally investigated compressibility effects on the large-scale coherent structures and their relation to turbulence statistics in compressible boundary layers. They found that compressibility has a clear effect on boundary layer, and that the scale of large-scale coherent structures based on the boundary layer thickness becomes longer and wider for supersonic turbulent boundary layers when compared with subsonic and transonic turbulent boundary layers. Due to the strong stabilising effect of stable density stratification, the existences of streamwise elongated low- and high-speed large-scale coherent structures were also confirmed in stably stratified shear layers by Watanabe *et al.* (2019) and Watanabe & Nagata (2021). These structures resemble turbulent structures found in wall turbulence. However, the compressibility effect on coherent structures in compressible mixing shear layers is not fully understood, particularly for the large-scale streaks of low- and high-speed streamwise velocity.

The purpose of this paper is to explore the compressibility effects on temporally evolving turbulent mixing layers at various Mach numbers. The characteristic of solenoidal and dilatational components of the velocity field is investigated by Helmholtz decomposition. Further understanding of the suppression mechanism of mixing layer growth rate is obtained by analysing the budgets of total TKE and the evolution of coherent structures. The properties of the large-scale structures are investigated through two-point correlations and conditionally averaging the turbulent fields, which are compared with the wall turbulence to reveal the universality of the large-scale structures in free shear and wall-bounded turbulent flows. The paper is organised as follows. The governing equations and computational method are provided in § 2, followed by a validation study in § 3. In § 4, we provide in detail our results. Finally, conclusions are drawn in § 5.

## 2. Governing equations and numerical method

The unsteady, three-dimensional, compressible Navier–Stokes equations in the conservative form are solved for the temporally evolving mixing layer, which are written as follows:

$$\frac{\partial \rho}{\partial t} + \frac{\partial (\rho u_k)}{\partial x_k} = 0, \tag{2.1}$$

$$\frac{\partial (\rho u_i)}{\partial t} + \frac{\partial (\rho u_k u_i)}{\partial x_k} = -\frac{\partial p}{\partial x_i} + \frac{1}{Re}\frac{\partial \sigma_{ik}}{\partial x_k}, \tag{2.2}$$

$$\frac{\partial E}{\partial t} + \frac{\partial [(E+p)u_j]}{\partial x_j} = \frac{1}{\alpha}\frac{\partial}{\partial x_k}\left(\kappa \frac{\partial T}{\partial x_k}\right) + \frac{1}{Re}\frac{\partial (u_j \sigma_{jk})}{\partial x_k}, \tag{2.3}$$

$$p = \rho T/(\gamma M^2), \tag{2.4}$$

where the indices $i = 1, 2, 3$ denote the three spatial directions represented by $x_1$, $x_2$ and $x_3$ (or $x$, $y$ and $z$), which are the streamwise, vertical and spanwise directions, respectively, and $u_1$, $u_2$ and $u_3$ (or $u$, $v$ and $w$) denote the instantaneous velocity components in the corresponding directions. Here, $\rho$ is instantaneous density, $p$ is instantaneous pressure and $T$ is instantaneous temperature. The viscous stress $\sigma_{ik}$ is defined as

$$\sigma_{ik} = 2\mu S_{ik} - \frac{2\mu \Theta}{3}\delta_{ik}, \tag{2.5}$$

in which $S_{ik} = (\partial u_i/\partial x_k + \partial u_k/\partial x_i)/2$ is the strain rate tensor, and $\Theta = \partial u_k/\partial x_k$ is the velocity divergence or dilatation. The total energy per unit volume $E$ is defined as

$$E = \frac{p}{\gamma - 1} + \frac{1}{2}\rho u_i u_i. \tag{2.6}$$

The temperature-dependent viscosity coefficient $\mu$ and thermal conductivity coefficient $\kappa$ are specified by Sutherland's law (Sutherland 1893).

The variables in the governing equations of compressible turbulence have been already normalised by a set of reference scales, including the reference length $L_r$, velocity $U_r$, density $\rho_r$, pressure $p_r = \rho_r U_r^2$, temperature $T_r$, energy per unit volume $\rho_r U_r^2$, viscosity $\mu_r$ and thermal conductivity $\kappa_r$ (Samtaney, Pullin & Kosović 2001; Wang *et al.* 2012). There are three reference governing parameters: the reference Reynolds number $Re = \rho_r U_r L_r/\mu_r$, the reference Mach number $M = U_r/c_r$ and the reference Prandtl number $Pr = \mu_r C_p/\kappa_r$, which is assumed to be equal to 0.7. In addition, the speed of sound is defined by $c_r = \sqrt{\gamma RT}$, where $R$ is the specific gas constant. Here $\gamma = C_p/C_v$ is the ratio of specific heat at constant pressure $C_p$ to that at constant volume $C_v$, which is assumed to be equal to 1.4. The parameter $\alpha$ is defined as $\alpha = Pr\,Re(\gamma - 1)M^2$.

The turbulent stress tensor $R_{ij}$ is defined by

$$R_{ij} = \bar{\rho}\widetilde{u_i'' u_j''} = \overline{\rho u_i'' u_j''}, \tag{2.7}$$

where $\tilde{\phi} = \overline{\rho\phi}/\bar{\rho}$ represents the Favre average of a variable $\phi$, and $\bar{\phi}$ is the Reynolds average obtained by plane averaging along the homogeneous $x$, $z$-directions and ensemble averaging of repeated simulations. The Reynolds fluctuations and Favre fluctuations are denoted as $\phi' = \phi - \bar{\phi}$ and $\phi'' = \phi - \tilde{\phi}$, respectively. The Reynolds stress is governed by

the following equation (Pantano & Sarkar 2002)

$$\frac{\partial R_{ij}}{\partial t} + \frac{\partial (R_{ij}\tilde{u}_k)}{\partial x_k} = T_{ij} + P_{ij} + \epsilon_{ij} + \Phi_{ij} + \Sigma_{ij}, \tag{2.8}$$

where the transport, turbulent production, dissipation, pressure–strain and mass flux coupling terms are, respectively,

$$T_{ij} = -\frac{\partial}{\partial x_k}\left(\overline{\rho u_i'' u_j'' u_k''} + \overline{p' u_j''}\delta_{ik} + \overline{p' u_i''}\delta_{jk} - \frac{1}{Re}\overline{\sigma_{ik}' u_j''} - \frac{1}{Re}\overline{\sigma_{jk}' u_i''}\right), \tag{2.9a}$$

$$P_{ij} = -R_{ik}\frac{\partial \tilde{u}_j}{\partial x_k} - R_{jk}\frac{\partial \tilde{u}_i}{\partial x_k}, \tag{2.9b}$$

$$\epsilon_{ij} = -\frac{1}{Re}\overline{\sigma_{ik}'\frac{\partial u_j''}{\partial x_k}} - \frac{1}{Re}\overline{\sigma_{jk}'\frac{\partial u_i''}{\partial x_k}}, \tag{2.9c}$$

$$\Phi_{ij} = \overline{p'\left(\frac{\partial u_j''}{\partial x_i} + \frac{\partial u_i''}{\partial x_j}\right)}, \tag{2.9d}$$

$$\Sigma_{ij} = \overline{u_j''}\left(\frac{1}{Re}\frac{\partial \bar{\sigma}_{ik}}{\partial x_k} - \frac{\partial \bar{p}}{\partial x_i}\right) + \overline{u_i''}\left(\frac{1}{Re}\frac{\partial \bar{\sigma}_{jk}}{\partial x_k} - \frac{\partial \bar{p}}{\partial x_j}\right). \tag{2.9e}$$

It is straightforward to obtain the transport equation for the TKE $\bar{K} = R_{ii}/2$ from (2.8) by contracting the indices

$$\frac{\partial \bar{K}}{\partial t} + \frac{\partial (\bar{K}\tilde{u}_k)}{\partial x_k} = \bar{T} + \bar{P} + \bar{\epsilon} + \bar{\Phi} + \bar{\Sigma}, \tag{2.10}$$

where the transport terms $\bar{T}$, $\bar{P}$, $\bar{\epsilon}$, $\bar{\Phi}$ and $\bar{\Sigma}$ are similarly obtained from (2.9), respectively,

$$\bar{T} = -\frac{\partial}{\partial x_k}\left(\frac{1}{2}\overline{\rho u_i'' u_i'' u_k''} + \overline{p' u_i''}\delta_{ik} - \frac{1}{Re}\overline{\sigma_{ik}' u_i''}\right), \tag{2.11a}$$

$$\bar{P} = -R_{ik}\frac{\partial \tilde{u}_i}{\partial x_k}, \tag{2.11b}$$

$$\bar{\epsilon} = -\frac{1}{Re}\overline{\sigma_{ik}'\frac{\partial u_i''}{\partial x_k}}, \tag{2.11c}$$

$$\bar{\Phi} = \overline{p'\frac{\partial u_i''}{\partial x_i}}, \tag{2.11d}$$

$$\bar{\Sigma} = \overline{u_i''}\left(\frac{1}{Re}\frac{\partial \bar{\sigma}_{ik}}{\partial x_k} - \frac{\partial \bar{p}}{\partial x_i}\right). \tag{2.11e}$$

The transport equations of the TKE components $\bar{K}_i$ can be simply obtained by avoiding summation convention over repeated indices $i$ in (2.10) and (2.11), and the corresponding transport terms are $\bar{T}_i$, $\bar{P}_i$, $\bar{\epsilon}_i$, $\bar{\Phi}_i$ and $\bar{\Sigma}_i$, which are omitted here for the sake of brevity (Pantano & Sarkar 2002; Ma & Xiao 2016; Arun *et al.* 2019).

The numerical simulation has been performed using an in-house code employing a hybrid numerical scheme proposed by Wang *et al.* (2010). The hybrid scheme combines a seventh-order weighted essentially non-oscillatory (WENO) scheme (Balsara & Shu 2000)

for the shocklet regions and an eighth-order compact central finite difference scheme (Lele 1992) for smooth regions. The shock front is identified by spatial points with highly negative local velocity divergence as defined by $\Theta < -3.0\Theta_{rms}$, where $\Theta_{rms} = \sqrt{\overline{\Theta^2}}$ is the root-mean-square (r.m.s.) value of velocity divergence. The time advancement is performed with a second-order explicit low-storage Runge–Kutta scheme as described by Gottlieb & Shu (1998). The stability and accuracy of the numerical method have been demonstrated in previous studies of compressible turbulence (Wang *et al.* 2010, 2012, 2018, 2019, 2020).

Figure 1 is a schematic of the flow configuration considered in the present work. In this figure, $x$ and $z$ represent the homogeneous streamwise and spanwise directions, respectively, and $y$ denotes the transverse direction. The vorticity thickness is computed by $\delta_\omega = \Delta U/(\mathrm{d}\bar{u}/\mathrm{d}y)_{max}$, and the momentum thickness, $\delta_\theta$, is defined as (Vreman *et al.* 1996)

$$\delta_\theta = \frac{1}{\rho_\infty \Delta U^2} \int_{-\infty}^{+\infty} \bar{\rho}(\Delta U/2 - \tilde{u})(\Delta U/2 + \tilde{u})\,\mathrm{d}y, \tag{2.12}$$

where $\Delta U$ is the free-stream velocity difference across the shear layer. The computational domain with lengths $L_x \times L_y \times L_z = 314\delta_\theta^0 \times 314\delta_\theta^0 \times 157\delta_\theta^0$ in the streamwise, transverse and spanwise directions is discretised uniformly with the number of grid points equal to $N_x \times N_y \times N_z = 1024 \times 1024 \times 512$, where $\delta_\theta^0$ is the initial momentum thickness. The plane $y = 0$ is at the centre of the computational domain. In order to allow periodic configuration in the vertical direction, the mean streamwise velocity is initialised by hyperbolic tangent profile with two shear layers (one is located at the middle and the other at the boundary of transverse direction),

$$\tilde{u}_1 = \frac{1}{2}\Delta U \left[ \tanh\left(\frac{y}{2C_\delta \delta_\theta^0}\right) - \tanh\left(\frac{y + L_y/2}{2C_\delta \delta_\theta^0}\right) + \tanh\left(\frac{y - L_y/2}{2C_\delta \delta_\theta^0}\right) \right], \tag{2.13}$$

where $C_\delta$ is an adjustment constant chosen such that the initial momentum thickness becomes $\delta_\theta^0$ for all simulations (Vaghefi & Madnia 2015). The mean vertical and spanwise velocities are set to zero, $\tilde{u}_2 = \tilde{u}_3 = 0$. The initial temperature is obtained from the Busemann–Crocco relationship (Ragab & Wu 1989; Arun *et al.* 2019) for compressible shear layers,

$$\mathcal{T} = 1 + \tfrac{1}{2}(\gamma - 1)M_c^2(1 - \tilde{u}_1^2), \tag{2.14}$$

where $M_c$ is the convective Mach number, defined as $M_c = \Delta U/(c_1 + c_2)$. Here $c_1$ and $c_2$ are the speed of sound in the upper and lower streams, respectively. The pressure field is uniform, and the density field is obtained from the ideal gas equation of state.

Note that the above initial mean field is periodic in all three directions, therefore triply periodic boundary condition is applied. Actually, by applying a numerical diffusion zone near the vertical edges of the computational domain, as shown in figure 1, the shear layer located at the boundary of vertical direction is forced to its initial state and the intensity of possible disturbances is sufficiently reduced such that there is negligible effect on the flow. The width of this buffer layer is set to $15\delta_\theta^0$ which is large enough for all cases presented in this paper. Additional discussions on the effects of the buffer layer width are provided in Appendix A. The periodic configuration is convenient for computing statistics and performing spectral analyses, and the accuracy of the present numerical simulation is validated by comparisons against previous simulations of temporally evolving mixing layers with stress-free boundary, as shown in § 3.

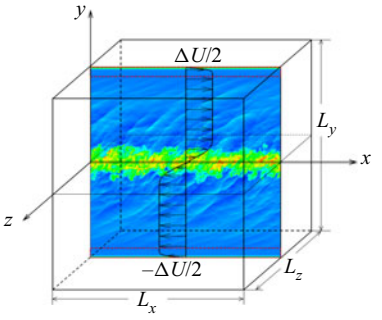


Figure 1. Schematic of the temporally evolving shear layer with mean velocity profile. The red dashed rectangles represent the extent of the sponge layers in vertical direction.

| Case | $M_c$ | $\tau$ | $M_t$ | $Re_\theta$ | $Re_\lambda$ | $Re_\omega$ | $\eta/\Delta x$ | $l_x/L_x$ | $l_z/L_z$ |
|---|---|---|---|---|---|---|---|---|---|
| M02 | 0.2 | $\tau_0 = 625$ | 0.10 | 3768 | 266 | 19 960 | 0.42 | 0.24 | 0.12 |
| | | $\tau_f = 875$ | 0.09 | 4798 | 292 | 25 166 | 0.46 | 0.28 | 0.14 |
| M08 | 0.8 | $\tau_0 = 750$ | 0.34 | 2990 | 202 | 17 230 | 0.49 | 0.32 | 0.08 |
| | | $\tau_f = 1250$ | 0.31 | 4546 | 236 | 26 028 | 0.56 | 0.49 | 0.10 |
| M18 | 1.8 | $\tau_0 = 1250$ | 0.65 | 3036 | 200 | 21 158 | 0.86 | 0.36 | 0.14 |
| | | $\tau_f = 2250$ | 0.57 | 5232 | 234 | 38 094 | 1.05 | 0.60 | 0.17 |

Table 1. Simulation parameters at the beginning ($\tau = \tau_0$) and end ($\tau = \tau_f$) of the self-similar period. Parameters $M_t$, $Re_\lambda$, $\eta$, $l_x$ and $l_z$ are obtained at $y = 0$.

In order to accelerate the transition to turbulence, a spatially correlated perturbation velocity field obtained by the digital filter method (Klein, Sadiki & Janicka 2003) is imposed on mean velocities with the length scales chosen as the vorticity thickness $\delta_\omega$ in each direction. It is assumed that the profiles of Reynolds stresses $R_{ij}$ have a Gaussian like distribution in $y$ to obey $R_{ij} = A(1 - \tilde{u}_1^2)$. The peak amplitude $A$ is set to $0.025\Delta U$ for the middle shear layer and there's no initial fluctuation in the boundary shear layer. Solenoidality is imposed on this initial turbulent field using Helmholtz decomposition of velocity fields (see (4.1) in § 4.2).

Numerical simulations are performed for three different values of convective Mach number, $M_c = 0.2, 0.8, 1.8$. The temporally evolving mixing layer is statistically homogeneous in the $x$ and $z$ directions. Therefore, the statistics are functions of $y$ and normalised time $\tau = t\Delta U/\delta_\theta^0$. Table 1 gives the key non-dimensional flow parameters corresponding to the self-similar stage at the centreline. The turbulent Mach number $M_t$ is defined by

$$M_t = \frac{\sqrt{2K}}{c}, \tag{2.15}$$

where $K$ is the TKE and $c$ is the average speed of sound. The turbulent Mach number ranges from 0.1 to 0.6, corresponding to the different levels of compressibility. The lowest turbulent Mach number case corresponds to a nearly incompressible condition, while the highest turbulent Mach number case almost approaches the strongest compressibility effects as reported in the literature, to the best of our knowledge.

The Reynolds numbers based on the momentum thickness $Re_\theta$, the vorticity thickness $Re_\omega$ and the Taylor microscale $Re_\lambda$ are defined as

$$Re_\theta = \frac{\rho_\infty \Delta U \delta_\theta}{\mu_\infty}, \quad Re_\omega = \frac{\rho_\infty \Delta U \delta_\omega}{\mu_\infty}, \quad Re_\lambda = 2K\sqrt{\frac{5\rho}{\mu\epsilon}}, \tag{2.16a–c}$$

respectively, where $\epsilon$ is the TKE dissipation rate per unit mass and $\mu$ is viscosity coefficient. The initial momentum thickness Reynolds number is $Re_\theta = 320$.

The Kolmogorov length scale $\eta$ is defined by

$$\eta = \left(\frac{\mu^3}{\rho^3\epsilon}\right)^{1/4}. \tag{2.17}$$

It is listed in table 1 that the resolution parameter $\eta/\Delta x$ is in the range $0.42 \leq \eta/\Delta x \leq 1.02$ at the centreline, where $\Delta x$ is the grid length in each direction, indicating that the resolution of the present simulations is fine enough to resolve down to the order of the Kolmorgorov length scale of the flow (Pantano & Sarkar 2002; Arun *et al.* 2019; Matsuno & Lele 2021). It is noted that the Kolmogorov length scale achieves its minimum value at the centreline, and it increases slightly during the self-similar region of the mixing layer, seeing the detailed analysis in § 4. Additional discussions on grid convergence are provided in Appendix A. The integral length scales in the streamwise direction ($l_x$) and spanwise direction ($l_z$) are defined as

$$l_x = \int_0^{L_x/2} \mathcal{R}_{uu}(r_x, 0, 0)\,\mathrm{d}r_x, \quad l_z = \int_0^{L_z/2} \mathcal{R}_{uu}(0, 0, r_z)\,\mathrm{d}r_z, \tag{2.18a,b}$$

respectively, where $\mathcal{R}_{ff}$ is the two-point correlation of a variable $f$, defined as

$$\mathcal{R}_{ff}(r_x, r_y, r_z) = \frac{\langle f'(x, 0, z) f'(x + r_x, r_y, z + r_z)\rangle}{f_{rms}^2}, \tag{2.19}$$

where $\langle\rangle$ stands for ensemble average. The largest integral length scales of $l_x/L_x = 0.60$ is obtained at the end of the self-similar region at $M_c = 1.8$, and it is nearly 3 times larger than the largest value in the previous numerical studies by Pantano & Sarkar (2002) and Vadrot, Giauque & Corre (2021), and comparable to that by Pirozzoli *et al.* (2015). The size of the computational domain is twice as large than those in previous numerical simulations (Pantano & Sarkar 2002; Arun *et al.* 2019; Vadrot, Giauque & Corre 2020; Matsuno & Lele 2021). Further analysis in § 4 shows that the integral length scales $l_x$ and $l_z$ are sufficiently small compared with the length of the computational domain, ensuring that the self-similar growth of large-scale structures is not confined. In order to enhance the statistical convergence, the horizontal averaging is complemented with an ensemble average over five independent runs with different initial conditions for each convective Mach number. Self-similar quantities are also time-averaged over the self-similar period.

## 3. Validation and general statistics

The purpose of this section is to validate our simulation by comparing present results against various previous experimental and numerical works in the literature. It is generally accepted that, after an initial transition period, the temporal mixing layer has a self-similar evolution characterised by a linear growth of momentum thickness. The selection of an appropriate self-similar range is a quite complex task because an exact self-similarity is

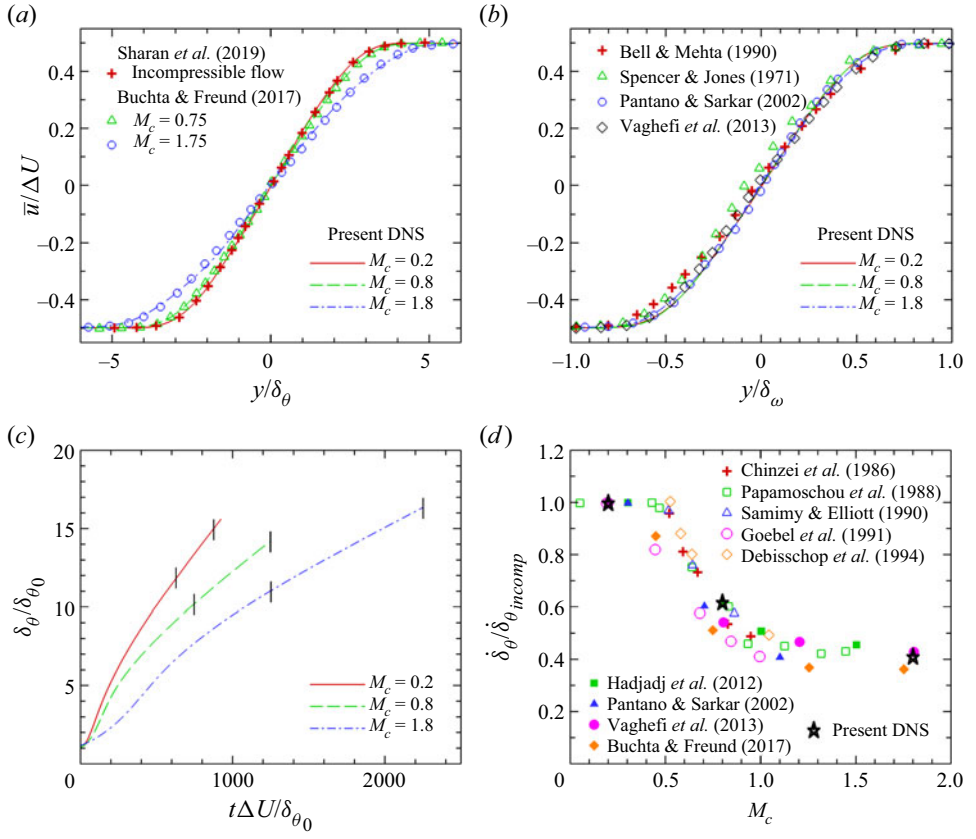


Figure 2. Comparison of mean streamwise velocity $\overline{u}/\Delta U$ in similarity coordinates (*a*) $y/\delta_\theta$ and (*b*) $y/\delta_\omega$. (*c*) Time evolution of normalised momentum thickness for different $M_c$, and the vertical line segments mark the self-similar time periods. (*d*) Comparison of linear growth rates at different $M_c$ with different numerical and experimental results.

difficult to achieve and there is no precise criteria to characterise this self-similar period. We determine the self-similar period by analysing the collapse of profiles of the mean velocity and the profiles of the Reynolds stresses, and further confirm it by computing the time evolution of the integrated transfer terms of TKE, as shown in § 4.3. The resulting time duration of the self-similar regime is indicated by intersecting vertical tick marks in figure 2(*c*) and reported in table 1.

Figures 2(*a*) and 2(*b*) show the mean streamwise velocity profile in similarity coordinates $y/\delta_\theta$ and $y/\delta_\omega$, respectively. Compared with several previous results (Spencer & Jones 1971; Bell & Mehta 1990; Pantano & Sarkar 2002; Vaghefi *et al.* 2013; Buchta & Freund 2017; Sharan, Matheou & Dimotakis 2019), very good agreement is obtained. We find that the mean streamwise velocity profiles at different convective Mach numbers collapse very well when plotted against $y/\delta_\omega$. The time evolution of the momentum thickness, normalised by its initial value ($\delta_\theta^0$), is shown in figure 2(*c*) for different $M_c$. It is observed that as the convective Mach number increases, the growth rates of both transitional and self-similar regimes decrease dramatically, leading to a longer transitional time, which is consistent with previous numerical results by Pantano & Sarkar (2002) and Vaghefi *et al.* (2013). The normalised self-similar growth rates are shown in

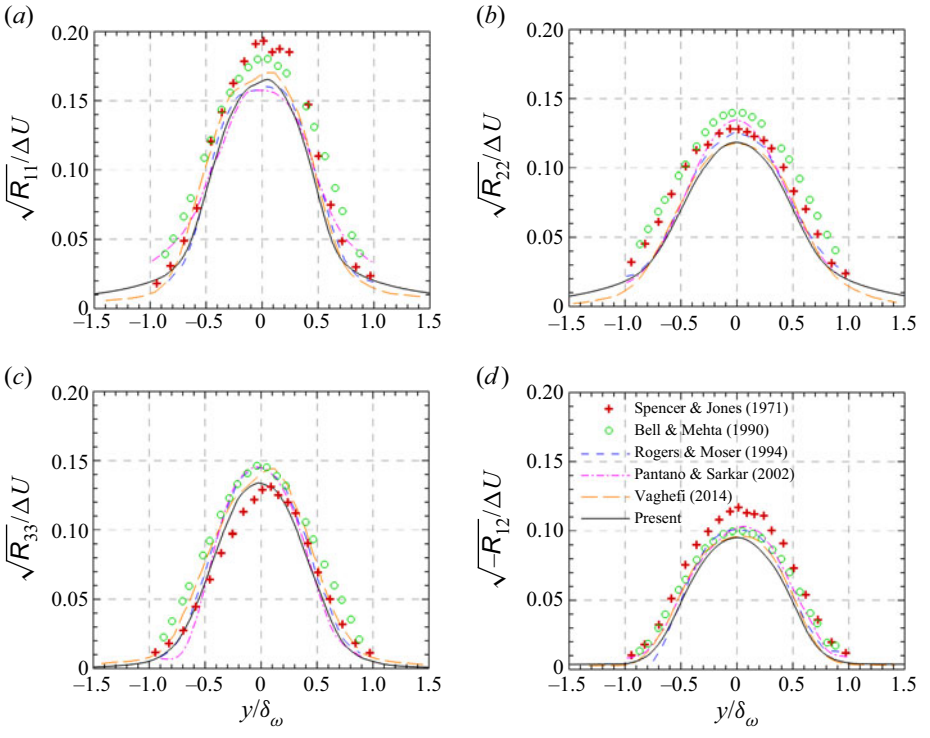


Figure 3. Comparison of normalised components of the Reynolds stress for case M02: (*a*) $\sqrt{R_{11}}/\Delta U$, (*b*) $\sqrt{R_{22}}/\Delta U$, (*c*) $\sqrt{R_{33}}/\Delta U$ and (*d*) $\sqrt{-R_{12}}/\Delta U$. The symbols denote experimental results for incompressible shear layers, and the curves represent numerical results. The legend is the same for all plots.

figure 2(*d*), where $\dot{\delta}_{inc}$ is the growth rate of the quasi-incompressible case $M_c = 0.2$ in our simulations. For comparison, the figure also shows available numerical (Pantano & Sarkar 2002; Hadjadj, Yee & Sjögreen 2012; Vaghefi *et al.* 2013; Buchta & Freund 2017) and experimental (Chinzei *et al.* 1986; Papamoschou & Roshko 1988; Samimy & Elliott 1990; Goebel & Dutton 1991; Debisschop, Chambers & Bonnet 1994) results in the literature.

The components of the normalised Reynolds stress are compared with previous works in figure 3 for the case M02. All variables are time-averaged over the self-similar region in similarity coordinates. It can be seen that the shape of the profiles and the peak value of Reynolds stresses are generally in good agreement with published results. For further validation of our DNS results, the dominant terms in the TKE transport equation (2.10), namely production, dissipation and transport terms, are compared with the previous results in figure 4 for cases M02, M08 and M18. These validations indicate that the current DNS provides an accurate representation of the compressible mixing layer during the self-similar stage.

## 4. Numerical results

### 4.1. *Local compressibility*

For compressible flow, the normalised velocity divergence serves as an excellent indicator of the local compressibility. To obtain an impression of the changes in the local compressibility of the mixing layer induced by convective Mach number, instantaneous

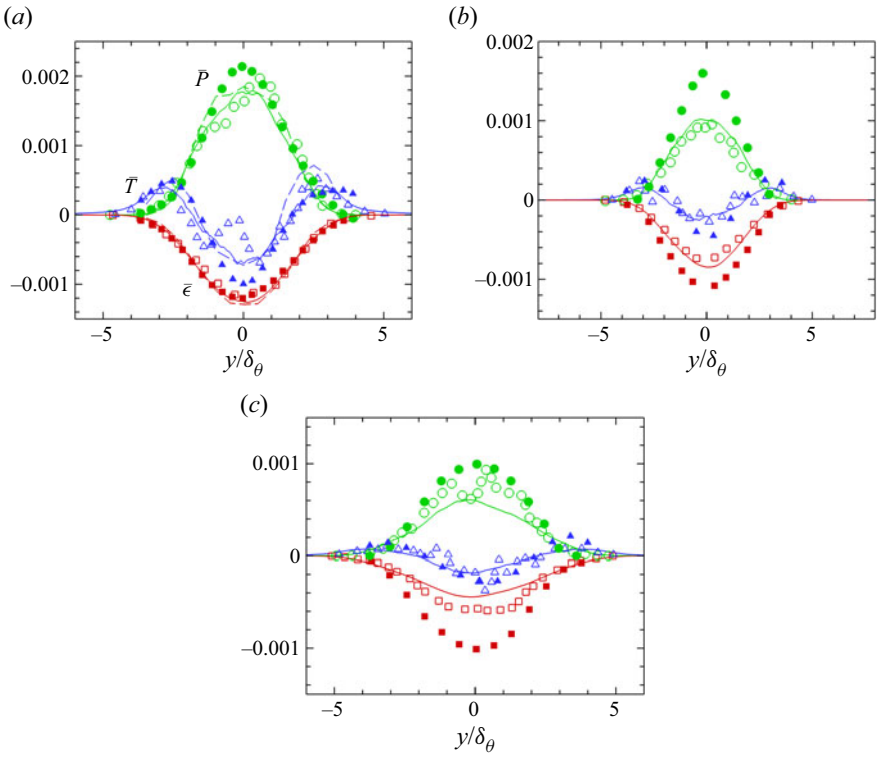


Figure 4. TKE transport equation terms in (2.10): $\bar{P}$ (green), $\bar{\epsilon}$ (red) and $\bar{T}$ (blue) for cases (*a*) M02, (*b*) M08 and (*c*) M18. The budget terms are normalised by $\Delta U^3/\delta_\theta$. The solid lines correspond to the present DNS. The dashed lines, open and filled symbols represent the results of Rogers & Moser (1994), Pantano & Sarkar (2002) and Vaghefi (2014), respectively.

fields of the normalised velocity divergence $\Theta\delta_\theta/\Delta U$ in the middle $x$–$y$ plane are shown in figure 5 at two different times, together with an isoline of vorticity magnitude $\omega = 0.01\Delta U/\delta_\theta^0$ selected as the nominal threshold to identify the turbulent–non-turbulent interface (TNTI) (Jahanbakhshi & Madnia 2016; Watanabe, Zhang & Nagata 2018). The vorticity magnitude is computed by $\omega = \sqrt{\omega_1^2 + \omega_2^2 + \omega_3^2}$, where $\omega_i$ are vorticity components. For the subsonic flow with $M_c = 0.2$, the results are omitted here because there is no obvious region of high compression. At $M_c = 0.8$, several shocklets can be seen outside the mixing zone at $\tau = 250$ in the transition region, whereas no shocklets are found at $\tau = 1000$ in the self-similar region. At $M_c = 1.8$, the shocklets can be observed during both transition and self-similar periods, and they tend to exhibit much smaller length scales inside the mixing layer, which is consistent with previous observations (Vaghefi *et al.* 2013; Buchta & Freund 2017).

To the best of the authors' knowledge, the appearance of shocklets in simulations of three-dimensional compressible mixing layers was first reported by Vreman, Kuerten & Geurts (1995). However, there has been no certain critical Mach number beyond which the shocklets appear. Wang, Gotoh & Watanabe (2017) found that the shocklets start to form when turbulent Mach number $M_t \geq 0.6$ in solenoidally forced compressible isotropic turbulence. Chen *et al.* (2018) observed shocklets at relatively smaller turbulent Mach numbers $M_t \geq 0.4$ in compressible homogeneous shear turbulence owing to the

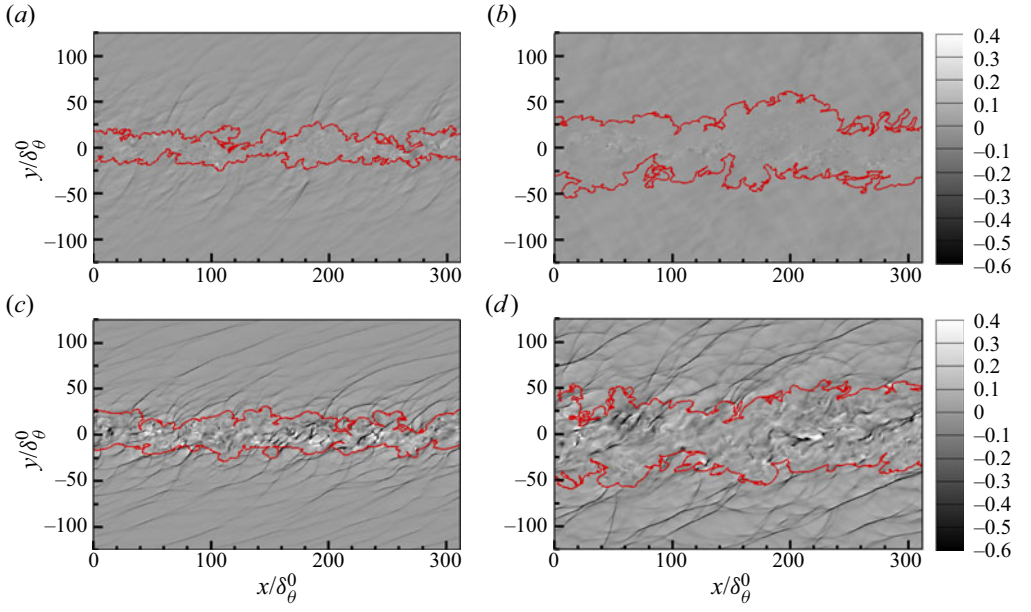


Figure 5. Visualisation of normalised velocity divergence $\Theta\delta_\theta/\Delta U$ in middle $x$–$y$ plane at two different time instants: (*a*) $M_c = 0.8$, $\tau = 250$, (*b*) $M_c = 0.8$, $\tau = 1000$, (*c*) $M_c = 1.8$, $\tau = 500$ and (*d*) $M_c = 1.8$, $\tau = 1250$. The red solid lines correspond to contours of $\omega = 0.01\Delta U/\delta_\theta^0$, showing the TNTI.

higher level of velocity fluctuation. In compressible mixing layers, the occurrence of shocklets has been captured when the convective Mach number is higher than 0.7 in two-dimensional simulations (Lele 1989). For most of the three-dimensional simulations, shocklets are observed at higher convective Mach number 1.2 (Vreman *et al.* 1995; Kourta & Sauvage 2002; Vaghefi 2014; Buchta & Freund 2017). It is noteworthy that Zhou *et al.* (2012) observed shocklets in the transition region of spatially developing compressible mixing layer at lower convective Mach number $M_c = 0.7$. They inferred that larger initial disturbance, which leads to stronger vortical structures, might contribute to the shocklet formation at this low convective Mach number.

In figure 6, we present the temporal evolutions of the centreline turbulent Mach number $M_{t,y0}$ and the r.m.s. velocity divergence $\Theta_{rms,y0}/(\Delta U/\delta_{\theta_0})$ for simulations with $M_c = 0.2$, 0.8 and 1.8. As can be seen, a significant overshoot in the centreline turbulent Mach numbers can be observed in the transitional region, as well as the centreline r.m.s. velocity divergence, indicating that the shocklet occurs more easily in this region. We find that the critical turbulent Mach number for shocklets to appear is close to $M_{t,y0} = 0.4$, which agrees well with that in compressible homogeneous shear turbulence (Chen *et al.* 2018), and the corresponding r.m.s. velocity divergence is $\Theta_{rms,y0}/(\Delta U/\delta_{\theta_0}) \approx 0.2$ for the free shear flow.

Figures 7(*a*) and 7(*b*) show the probability density function (PDF) of the normalised velocity divergence inside and outside the turbulent region at several time instants for convective Mach number $M_c = 0.8$. It was shown in previous results that the PDF of velocity divergence became more skewed towards the negative value as the turbulent Mach number and Taylor Reynolds number increase, due to strong compression region associated with shocklets which occurs much more frequently than the strong expansion region (Wang *et al.* 2012; Vaghefi & Madnia 2015; Chen *et al.* 2019). For the moderately

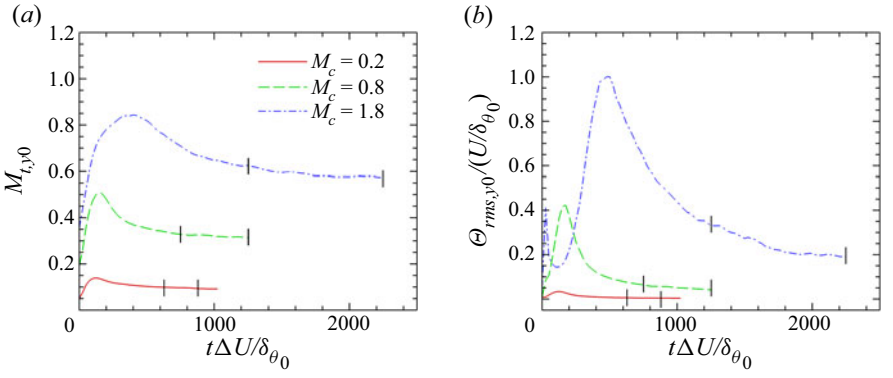


Figure 6. Temporal evolution of the centreline (*a*) turbulent Mach number $M_{t,y0}$ and (*b*) r.m.s. velocity divergence $\Theta_{rms,y0}/(\Delta U/\delta_{\theta_0})$ at the centreplane for simulations with $M_c = 0.2$, 0.8 and 1.8. The dashed vertical lines mark the self-similar time periods.

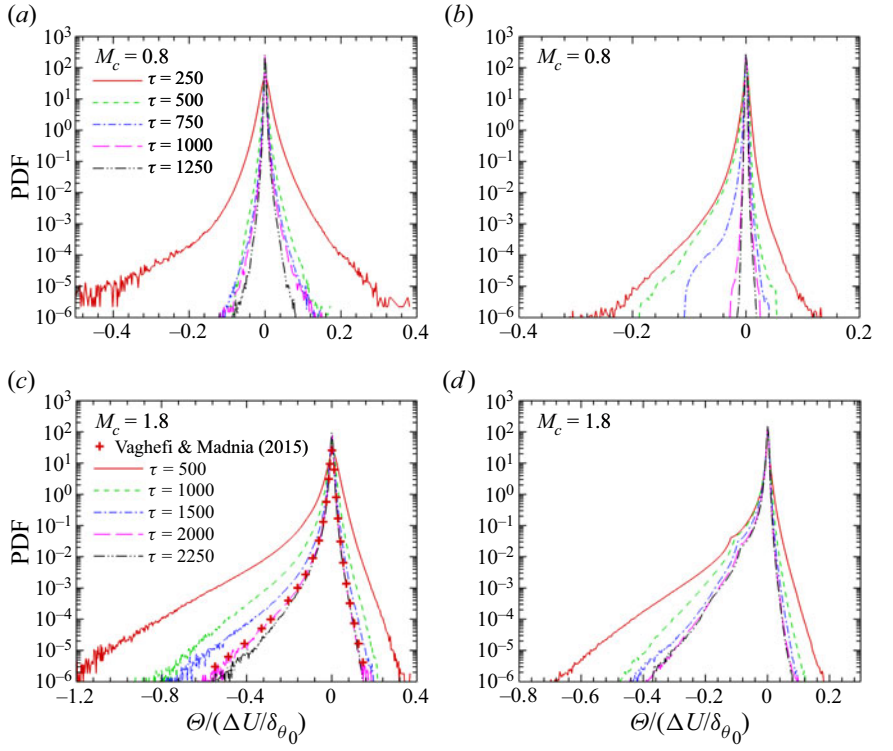


Figure 7. PDF of the normalised velocity divergence $\Theta/(\Delta U/\delta_{\theta_0})$ at five different time instants (*a*),(*c*) in the turbulent region and (*b*),(*d*) outside the turbulent region for cases at (*a*),(*b*) $M_c = 0.8$ and (*c*),(*d*) $M_c = 1.8$.

compressible case with $M_c = 0.8$, the PDF of velocity divergence in the turbulent region exhibits a skewness toward the negative side only at transition period $\tau = 250$, and then it rapidly becomes nearly symmetric. The PDF of velocity divergence outside the turbulent region is skewed toward the negative side until $\tau = 750$ in the self-similar period, owing to the shocklets radiated from the mixing zone.

Figures 7(*c*) and 7(*d*) show the PDF of the normalised velocity divergence inside and outside the turbulent region at several time instants for convective Mach number $M_c = 1.8$. As we can see, the PDFs of velocity divergence both inside and outside the turbulent region are always strongly skewed towards the negative values. At $\tau = 2000$, the PDF of velocity divergence inside the turbulent region is in excellent agreement with the result of Vaghefi & Madnia (2015) which is sampled at the beginning of the self-similar evolution. The two tails of PDF become shorter as time goes on, indicating that the local compressibility continuously decreases. We also find that the two tails of PDF inside the turbulent region are always longer than that outside the turbulent region, showing stronger local compressibility in the mixing zone.

### 4.2. *Helmholtz decomposition of velocity fields*

To reveal the underlying physics in the compressible turbulence and specifically the characteristic of local compressibility, we shall employ the well-known Helmholtz decomposition (Erlebacher & Sarkar 1993; Samtaney *et al.* 2001; Wang *et al.* 2012) to the velocity field

$$\boldsymbol{u} = \boldsymbol{u}_s + \boldsymbol{u}_d, \tag{4.1}$$

where the solenoidal component $\boldsymbol{u}_s$ satisfies $\boldsymbol{\nabla} \cdot \boldsymbol{u}_s = 0$ and the dilatational component $\boldsymbol{u}_c$ is irrotational, i.e. $\boldsymbol{\nabla} \times \boldsymbol{u}_d = 0$.

The instantaneous fields of decomposed velocity in the $x$–$y$ plane at $z = L_z/2$ are presented in figures 8 and 9 for the cases with $M_c = 0.8$ at $\tau = 1000$ and $M_c = 1.8$ at $\tau = 1700$, respectively. Note that all visualisations are selected at the middle of the self-similar region. For solenoidal velocity component, the visualisations in figures 8(*a*),(*c*),(*e*) and 9(*a*),(*c*),(*e*) show the typical features of a turbulent mixing layer, with patches of mixed fluid in the central region entraining patches of unmixed fluid from both external streams. It can be seen that the $u_s''$ field in the $x$–$y$ plane is characterised by elongated low- and high-speed regions, with characteristic sizes of the order of $\delta_\omega$. Comparing figures 8(*a*) and 8(*c*) or figures 9(*a*) and 9(*c*) reveals a strong anticorrelation between $u_s''$ and $v_s''$ events. The large-scale negative $u_s''$ events are characterised by regions of positive $v_s''$, upraising the low-speed fluid. The large-scale positive $u_s''$ events are accompanied by regions of negative $v_s''$, moving the high-speed fluid downwards. Moreover, the solenoidal velocity fields become visibly smoother at small scales for higher convective Mach number $M_c = 1.8$. Figures 10 and 11 show the instantaneous fields of decomposed velocity in $x$–$z$ plane at $y = 0$ for cases with $M_c = 0.8$ at $\tau = 1000$ and $M_c = 1.8$ at $\tau = 1700$, respectively. The main characteristic of the solenoidal velocity field is consistent with that found previously in the $x$–$y$ plane. The presence of large-scale streamwise elongated streaks of $u_s''$ is presented more clearly in the $x$–$z$ plane visualisation, with spanwise sizes of about $L_z/4$ in the self-similar state. This indicates that the spanwise length of the domain is large enough for the present simulation.

As can be seen in the right subfigures of figures 8 to 11, the increasing of convective Mach number induces different flow patterns of dilatational velocity component both in the $x$–$y$ and $x$–$z$ planes. For the case with $M_c = 0.8$, all three dilatational velocity components exhibit large block-like spatial structures. The $u_d''$ and $v_d''$ structures are aligned at oblique angles to the streamwise direction in $x$–$y$ plane, whereas the $w_d''$ structure is almost perpendicular. The $v_d''$ and $w_d''$ structures extend over the entire spanwise length of the domain, as shown in figures 10(*d*) and 10(*f*). These results suggest the presence of the spanwise rollers at $M_c = 0.8$, which also can be observed in the instantaneous fields of solenoidal velocity in the $x$–$y$ plane, as shown in figures 8(*a*), 8(*c*) and 8(*e*).

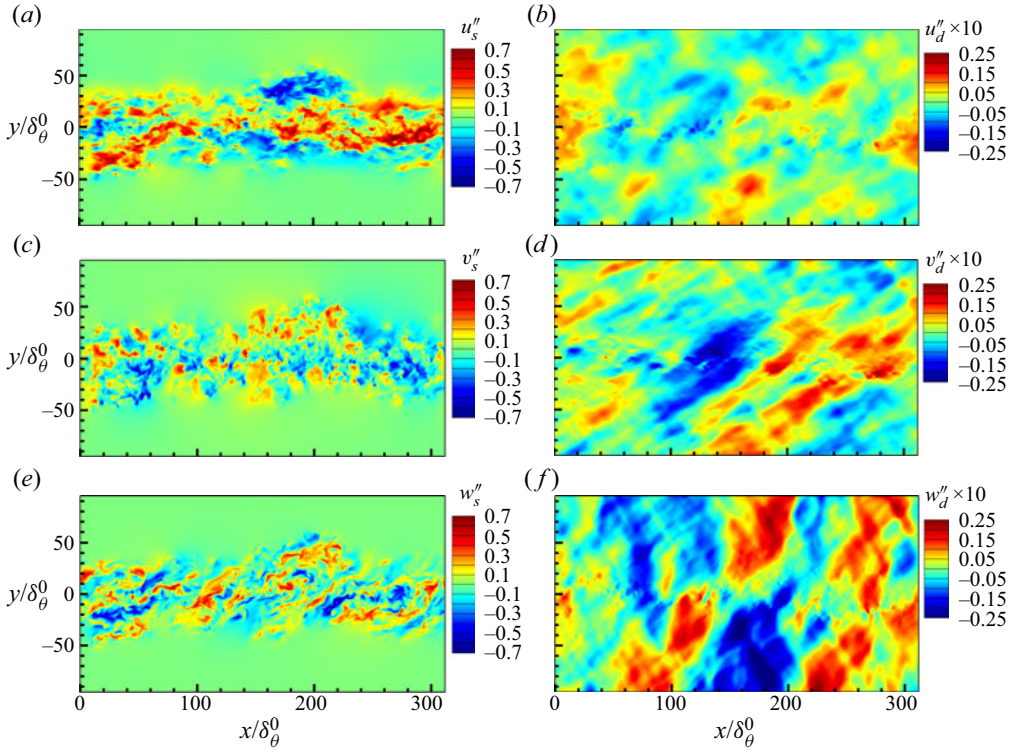


Figure 8. Instantaneous fields of (*a*) $u_s''$, (*b*) $u_d''$, (*c*) $v_s''$, (*d*) $v_d''$, (*e*) $w_s''$ and (*f*) $w_d''$ in the central $x$–$y$ plane for case M08 at $\tau = 1000$.

At convective Mach number $M_c = 1.8$, all three dilatational velocity components show severe discontinuity at the position of shocklets, particularly in the non-turbulent region, as presented in figures 9(*b*), 9(*d*) and 9(*f*). As can be seen, the fluids on two sides of shocklets move towards the shocklets and generate a sheet-like strong compressible region, causing a strong anticorrelation between $u_d''$ and $v_d''$ events. In the middle $x$–$z$ plane, the $u_d''$ and $v_d''$ events are also anticorrelated, which becomes less apparent masked by the trivial spanwise structures of $u_d''$.

To have a better picture of the effect of convective Mach number on the correlation between streamwise and vertical velocity components, we present the joint PDF of the velocity components, computed inside and outside the turbulent region at an instant in the self-similar region. As shown in figure 12(*a*), the joint PDF of $u_s''/u_{s,rms}''$ and $v_s''/v_{s,rms}''$ in the turbulent region reveals a statistical preference for points in the second and fourth quadrants, appearing as the oval contour lines. The long axis of the oval shape of PDF($u_s''$, $v_s''$) exhibits an inclined angle with the symmetry line of the $u_s''$–$v_s''$ plane, indicating the component anisotropy of solenoidal velocity components. This oval shape of the PDF($u_s''$, $v_s''$) is consistent well with that in incompressible homogeneous shear flow (Adrian & Moin 1988) and different from the results in the wall-bounded turbulent flow where axisymmetric shapes are usually observed (Wallace 2016; Yu, Xu & Pirozzoli 2019; Xu *et al.* 2021*a*). PDF($u_s''$, $v_s''$) in the non-turbulent region decays rapidly, illustrating the solenoidal velocity components are insignificant here, as can be seen from figure 12(*b*).

The joint PDFs of $u_d''/u_{d,rms}''$ and $v_d''/v_{d,rms}''$ are plotted in figures 12(*c*) and 12(*d*). In the turbulent region, we find that there is no significant correlation between $u_d''$ and $v_d''$

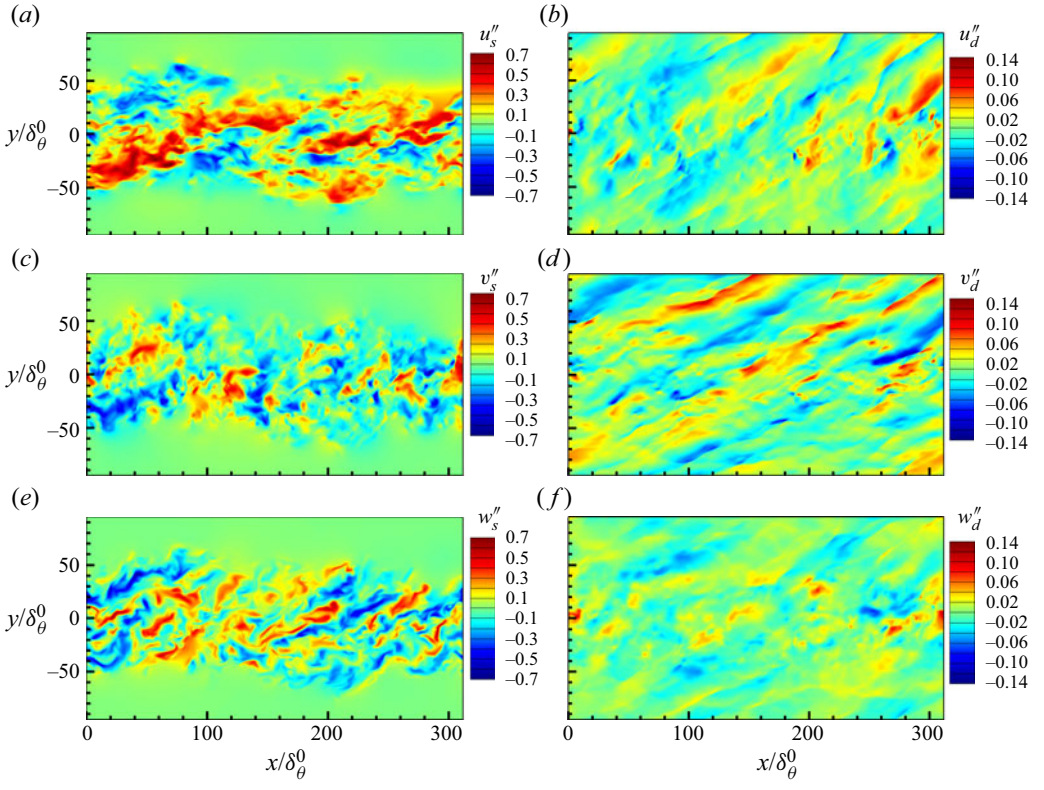


Figure 9. Instantaneous fields of (*a*) $u_s''$, (*b*) $u_d''$, (*c*) $v_s''$, (*d*) $v_d''$, (*e*) $w_s''$ and (*f*) $w_d''$ in the central $x$–$y$ plane for the case M18 at $\tau = 1700$.

for $M_c = 0.8$, whereas PDF($u_d''$, $v_d''$) also has a statistical preference in the second and fourth quadrants for $M_c = 1.8$, showing an oval shape similar to that of PDF($u_s''$, $v_s''$). In the non-turbulent region, both for $M_c = 0.8$ and $M_c = 1.8$, PDF($u_d''$, $v_d''$) has the inclined oval pattern, which is elongated in the $u_d''$ direction for $M_c = 1.8$ compared with that in the turbulent region. Actually, we find that, as the development of turbulent flow, the inclination angle of the oval shape of the PDF($u_d''$, $v_d''$) for $M_c = 0.8$ in non-turbulent region increases monotonically from 10° at $\tau = 200$ to nearly 30° at $\tau = 1000$. Only the results at $\tau = 1000$ is illustrated here in figure 12(*d*) for brevity.

It is worth noting that the statistical preference in the second and fourth quadrants of PDF($u_s''$, $v_s''$) and PDF($u_d''$, $v_d''$) corresponds to totally different physical processes. The former is related to the mixing between the two streams, demonstrated in the left subfigures of figures 8–11, resembling the sweep and ejection events in wall-bounded turbulent shear flow, and the latter is due to the induction of strong compression or expansion motions, seen from the right subfigures of figures 8–11.

On the basis of Helmholtz decomposition of velocity, the Reynolds stress $R_{ij}$ can be decomposed into

$$R_{ij} = \overline{\rho u_i'' u_j''} = \overline{\rho u_{s,i}'' u_{s,j}''} + \overline{\rho u_{d,i}'' u_{d,j}''} + \overline{\rho u_{s,i}'' u_{d,j}''} + \overline{\rho u_{d,i}'' u_{s,j}''}. \tag{4.2}$$

However, it is found that in the turbulent region the magnitudes of the last three terms on the right-hand side of (4.2) are several orders of magnitude smaller than the first term, even for the highest convective Mach number $M_c = 1.8$. Then we take Reynolds shear

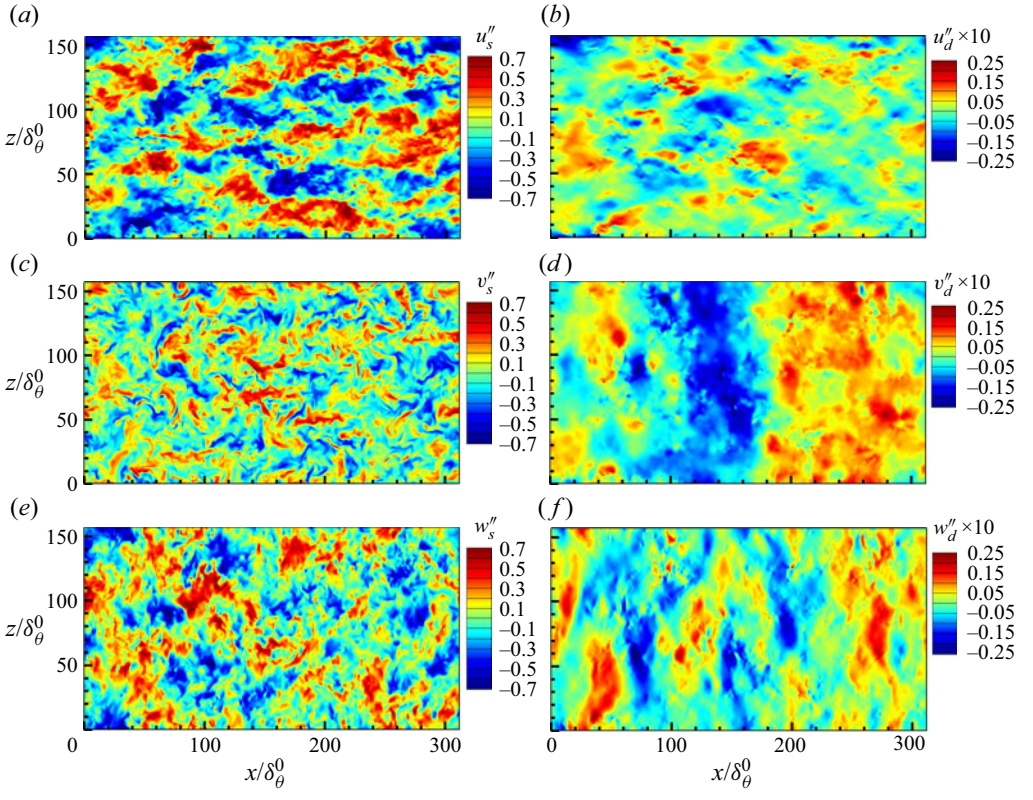


Figure 10. Instantaneous fields of (*a*) $u_s''$, (*b*) $u_d''$, (*c*) $v_s''$, (*d*) $v_d''$, (*e*) $w_s''$ and (*f*) $w_d''$ in the central $x$–$z$ plane for case M08 at $\tau = 1000$.

stress $R_{12} = \overline{\rho u'' v''}$ for example to show the effect of compressibility, and the Helmholtz decomposition of Reynolds normal stresses $R_{11}$, $R_{22}$ and $R_{33}$ can be found in Appendix B. The statistical preference in the second and fourth quadrants of PDF($u_s''$, $v_s''$) and PDF($u_d''$, $v_d''$) above shows that both solenoidal and dilatational velocity have a contribution to the negative values of the Reynolds shear stress. Figure 13 provides the Reynolds shear stress and its decomposed components for cases with $M_c = 0.8$ and $M_c = 1.8$. We can see that $R_{ij}$ and $\overline{\rho u_s'' v_s''}$ overlap almost perfectly with each other for both $M_c = 0.8$ and $M_c = 1.8$, indicating the dominant role of the solenoidal velocity field. For $M_c = 0.8$, $\overline{\rho u_s'' v_d''}$ is positive with a peak value at $y = 0$ and is significantly greater than the negligible two terms $\overline{\rho u_d'' v_d''}$ and $\overline{\rho u_d'' v_s''}$. For $M_c = 1.8$, the values of three dilatation-related terms are on the same order. As the convective Mach number increases, the magnitudes of three dilatation-related terms become larger, demonstrating the effect of compressibility. It is interesting to note that for $M_c = 1.8$, $\overline{\rho u_d'' v_d''}$ has two peak values at $y/\delta_\omega \approx \pm 0.5$ and becomes larger than $\overline{\rho u_s'' v_s''}$ in the non-turbulent region, which is probably due to the induction of the shocklets frequently formed near the TNTI, consistent with the analysis of figure 9.

### 4.3. *Integrated TKE transport*

The physical mechanism of the suppression of layer growth rate due to compressibility is further examined by analysing the time evolution of integrated TKE transport. The terms

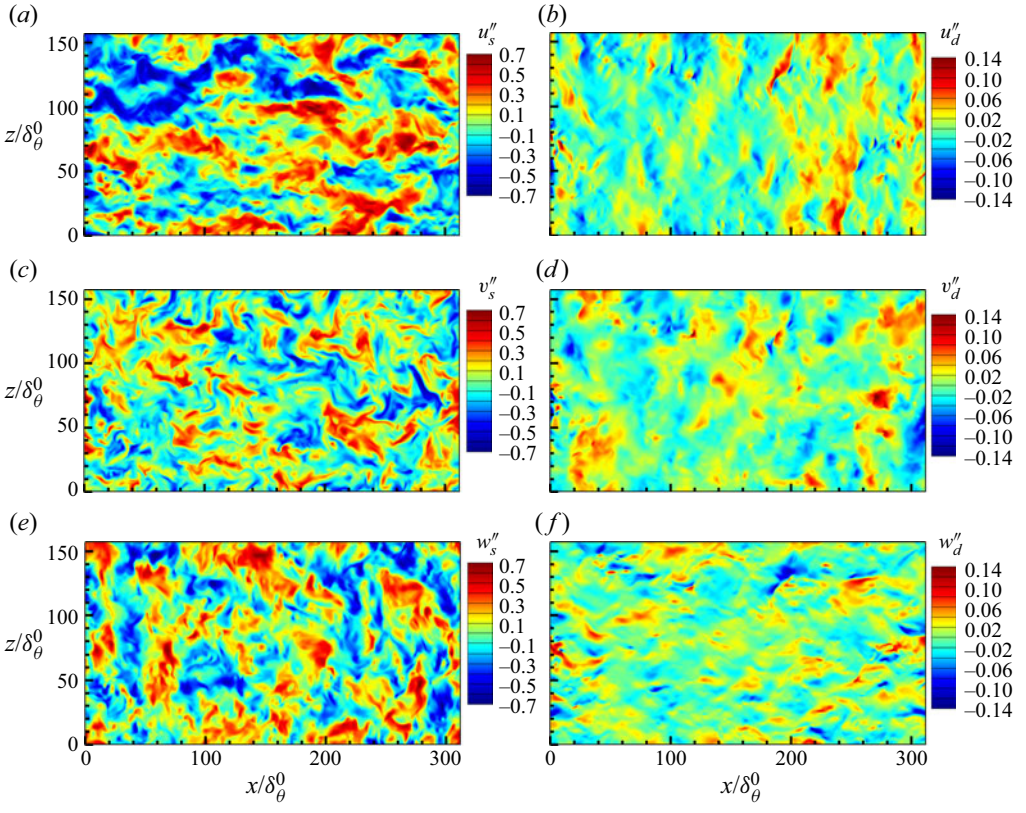


Figure 11. Instantaneous fields of (*a*) $u_s''$, (*b*) $u_d''$, (*c*) $v_s''$, (*d*) $v_d''$, (*e*) $w_s''$ and (*f*) $w_d''$ in the central $x$–$z$ plane for case M18 at $\tau = 1700$.

in conservative form disappear after integration, hence the equation of the $y$-integrated TKE becomes (Vreman *et al.* 1996; Attili & Bisetti 2012)

$$\frac{\partial \hat{K}}{\partial t} = \hat{P} + \hat{\epsilon} + \hat{\Phi} + \hat{\Sigma}, \tag{4.3}$$

where

$$\hat{K} = \int_{-L_y/2}^{L_y/2} \frac{1}{2}\overline{\rho u_i'' u_i''}\,\mathrm{d}y, \tag{4.4}$$

is total TKE, and the integrated transport terms $\hat{P}$, $\hat{\epsilon}$, $\hat{\Phi}$ and $\hat{\Sigma}$ are

$$\hat{P} = -\int_{-L_y/2}^{L_y/2} R_{ik}\frac{\partial \tilde{u}_i}{\partial x_k}\,\mathrm{d}y, \tag{4.5a}$$

$$\hat{\epsilon} = -\int_{-L_y/2}^{L_y/2} \frac{1}{Re}\overline{\sigma_{ik}'\frac{\partial u_i''}{\partial x_k}}\,\mathrm{d}y, \tag{4.5b}$$

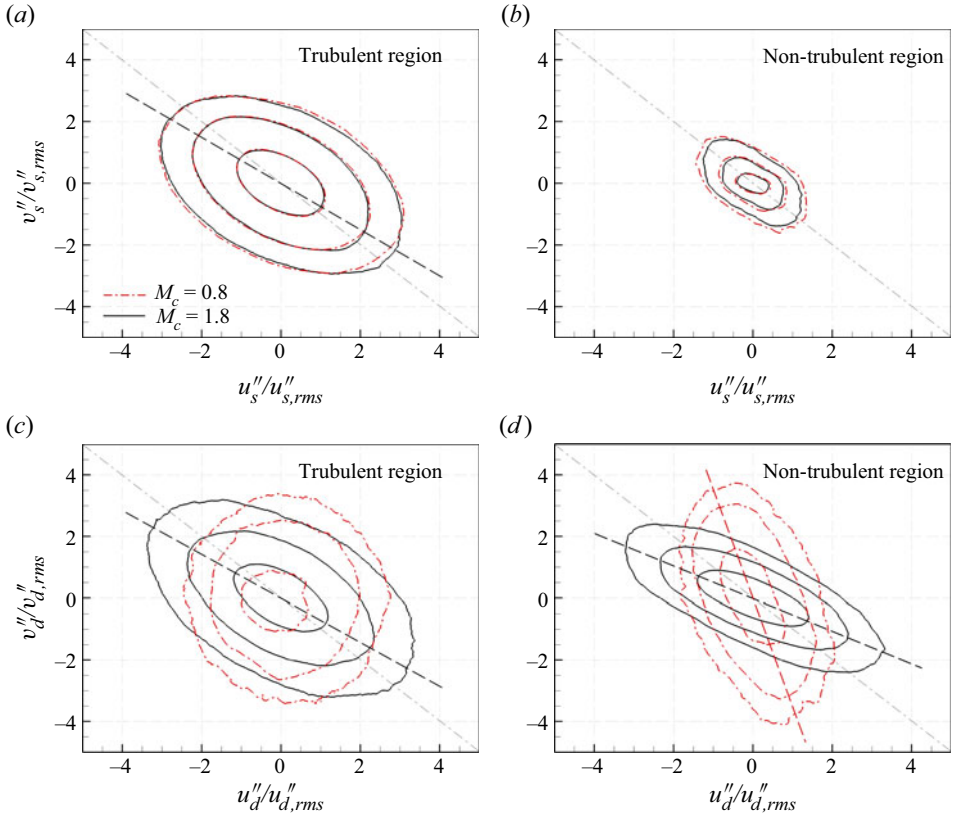


Figure 12. Joint PDF of (*a*),(*b*) $u_s''/u_{s,rms}''$ and $v_s''/v_{s,rms}''$ and (*c*),(*d*) $u_d''/u_{d,rms}''$ and $v_d''/v_{d,rms}''$ for case with $M_c = 0.8$ at $\tau = 1000$ and $M_c = 1.8$ at $\tau = 1250$: (*a*),(*c*) in the turbulent region and (*b*),(*d*) in the non-turbulent region. The thick dashed auxiliary line indicates the long axis of the oval shape. The thin dashed-dotted line represents the symmetry line of the $u_s''$–$v_s''$ plane. The contour levels 0.001, 0.01 and 0.1 are shown.

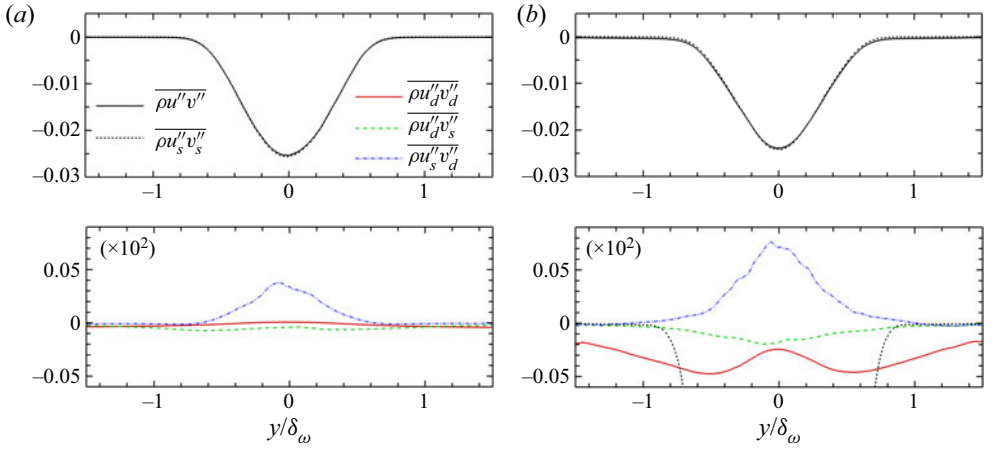


Figure 13. The Reynolds shear stress and its decomposed components for cases with (*a*) $M_c = 0.8$ and (*b*) $M_c = 1.8$. The legend is the same for both plots.

$$\hat{\Phi} = \int_{-L_y/2}^{L_y/2} \overline{p' \frac{\partial u_i''}{\partial x_i}}\, \mathrm{d}y, \tag{4.5c}$$

$$\hat{\Sigma} = \int_{-L_y/2}^{L_y/2} \overline{u_i''} \left( \frac{1}{Re} \frac{\partial \bar{\sigma}_{ik}}{\partial x_k} - \frac{\partial \bar{p}}{\partial x_i} \right) \mathrm{d}y. \tag{4.5d}$$

The magnitude of the integrated mass flux coupling term is still negligible. The transport equations of the integrated TKE components $\hat{K}_i$ and the Reynolds shear stress $\hat{R}_{12}$ can be obtained similarly, which are omitted here for brevity.

Figure 14 displays the time evolution of the normalised $y$-integrated TKE $\hat{K}/\Delta U^2$, its three components $\hat{K}_i/\Delta U^2$ and the Reynolds shear stress $\hat{R}_{12}/\Delta U^2$ at $M_c = 0.2$, 0.8 and 1.8. We can see that the integrated TKE and Reynolds shear stress grow linearly after a rapid growing transition region with a slight overshoot between two regions only at $M_c = 0.8$. Because of the anisotropic nature of free shear flows, it is generally observed that the components of integrated TKE satisfy the relationship $\hat{K}_1 > \hat{K}_3 > \hat{K}_2$ in the self-similar region. It is interesting for $M_c = 0.2$ that the vertical component $\hat{K}_2$ of the TKE is larger than the spanwise component $\hat{K}_3$ in transition region $\tau < 150$, and undergoes an accelerating growth resulting in $\hat{K}_2 > \hat{K}_3$ again beyond the self-similar region $\tau > 750$, as shown in figure 14(*a*). This behaviour is consistent with a previous numerical study of a spatially developing incompressible mixing layer by Attili & Bisetti (2012). We observe that the rapid growth of $\hat{K}_2$ in the late stages of development at $M_c = 0.2$ is the characteristic of the larger spanwise rollers generated by the Kelvin–Helmholtz instability, which is in agreement with previous results by Rogers & Moser (1994).

Figure 15 displays the time evolution of the normalised $y$-integrated production $\hat{P}/\Delta U^3$, dissipation $\hat{\epsilon}/\Delta U^3$ and pressure–strain $\hat{\Phi}/\Delta U^3$ in the equation of $\hat{K}$ at $M_c = 0.2$, $M_c = 0.8$ and $M_c = 1.8$. Here, the integrated mass flux coupling and transport terms have been neglected because their magnitude is very small, even in the large $M_c$ case. At $M_c = 0.2$, the asymptotic behaviour of $\hat{P}/\Delta U^3$ and $\hat{\epsilon}/\Delta U^3$ is in good agreement with the previous numerical results by Attili & Bisetti (2012) in a spatially evolving incompressible mixing layer, as compared in figure 15(*b*) where the abscissa is a local Reynolds number $Re_\omega = \rho_\infty \Delta U \delta_\omega / \mu_\infty$, which allows a direct comparison between the spatially and temporally evolving mixing layers. As convective Mach number increases, both magnitudes of the integrated production and dissipation become smaller, whereas the integrated pressure–strain term slightly increases only in the transition region. We can see that the integrated pressure–strain term is always much smaller than the other two terms, indicating that the net contribution of pressure dilatation to the kinetic energy transfer is negligibly small. This is consistent with previous studies on compressible turbulence (Wang *et al.* 2018, 2021). In the transition region, $\hat{P}/\Delta U^3$ grows linearly for all three convective Mach numbers. In contrast, $\hat{\epsilon}/\Delta U^3$ grows linearly only at $M_c = 1.8$ and it satisfies $\hat{\epsilon}/\Delta U^3 \propto -\tau^2$ at $M_c = 0.2$ and $M_c = 0.8$. An overshoot in the integrated production and dissipation occurs near the end of the transition region, and then the overshoot decays and becomes nearly a constant in the self-similar region. We also observe that the dissipation overshoot clearly lags behind the production overshoot. The ratio between the corresponding time of the dissipation overshoot $\tau_\epsilon$ and the production overshoot $\tau_P$ is defined to measure the lag level between them. The values for $\tau_\epsilon/\tau_P$ are 1.8, 1.5 and 1.2 at $M_c = 0.2$, $M_c = 0.8$ and $M_c = 1.8$, respectively. This result indicates that the dissipation starts to effectively balance the production earlier for larger convective

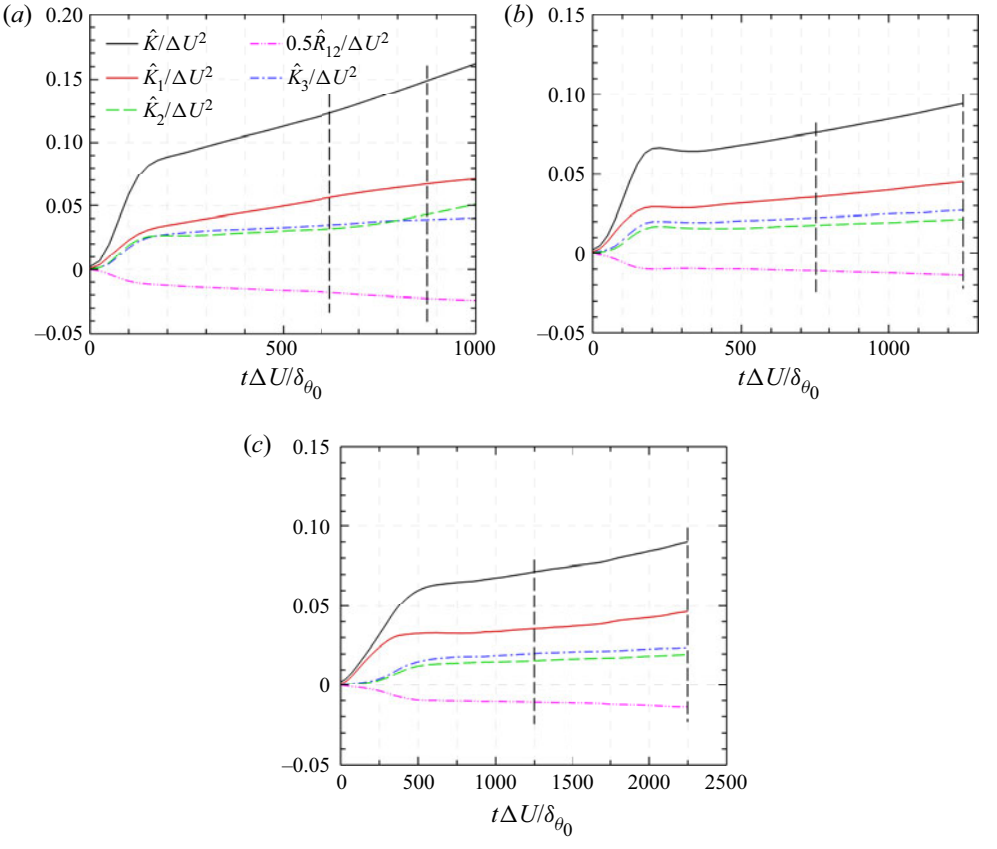


Figure 14. Time evolution of $\hat{K}/\Delta U^2$, $\hat{K}_i/\Delta U^2$, $0.5\hat{R}_{12}/\Delta U^2$ at (*a*) $M_c = 0.2$, (*b*) $M_c = 0.8$ and (*c*) $M_c = 1.8$. The legend is the same for all plots. The dashed vertical lines mark the self-similar time periods.

Mach number, and partly reveals some reasons for reduction of growth rate with increased convective Mach number in the transition region.

In order to better understand the effect of compressibility, we plot the time evolution of transport terms for $\hat{K}_i$ in figure 16. In all cases, we can see that the production terms associated with $\hat{K}_2$ and $\hat{K}_3$, namely $\hat{P}_2$ and $\hat{P}_3$, are negligible concerning the $\hat{K}_1$ production $\hat{P}_1$. As is well known, on average, the pressure–strain correlation components $\hat{\Phi}_i$ redistribute energy from $\hat{K}_1$ to the other components $\hat{K}_2$ and $\hat{K}_3$. Figure 16(*a*) shows that $\hat{\Phi}_2 > \hat{\Phi}_3$ for $\tau < 100$ and $\tau > 700$, leading to the preferential transfer of energy into the vertical velocity fluctuation, as shown in figure 14(*a*). It is interesting to note that all pressure–strain correlation components $\hat{\Phi}_i$ and production almost reach their peak values at the same time for all three convective Mach numbers.

For the case with $M_c = 0.2$, the three components of viscous dissipation $\hat{\epsilon}_i$ always overlap perfectly with each other, as shown in figure 16(*a*), suggesting local isotropy of the flow at small scales. As the convective Mach number increases, the viscous dissipation occurs more anisotropically and is dominated by the streamwise component $\hat{\epsilon}_1$ in the transition region. As is clearly presented in figure 16(*c*) for $M_c = 1.8$, the magnitude of streamwise component $\hat{\epsilon}_1$ is found to be even larger than $\hat{\Phi}_1$, whereas the $\hat{\epsilon}_2$ and $\hat{\epsilon}_3$ components are still proportional to $-\tau^2$, resulting in linear growth of the total viscous

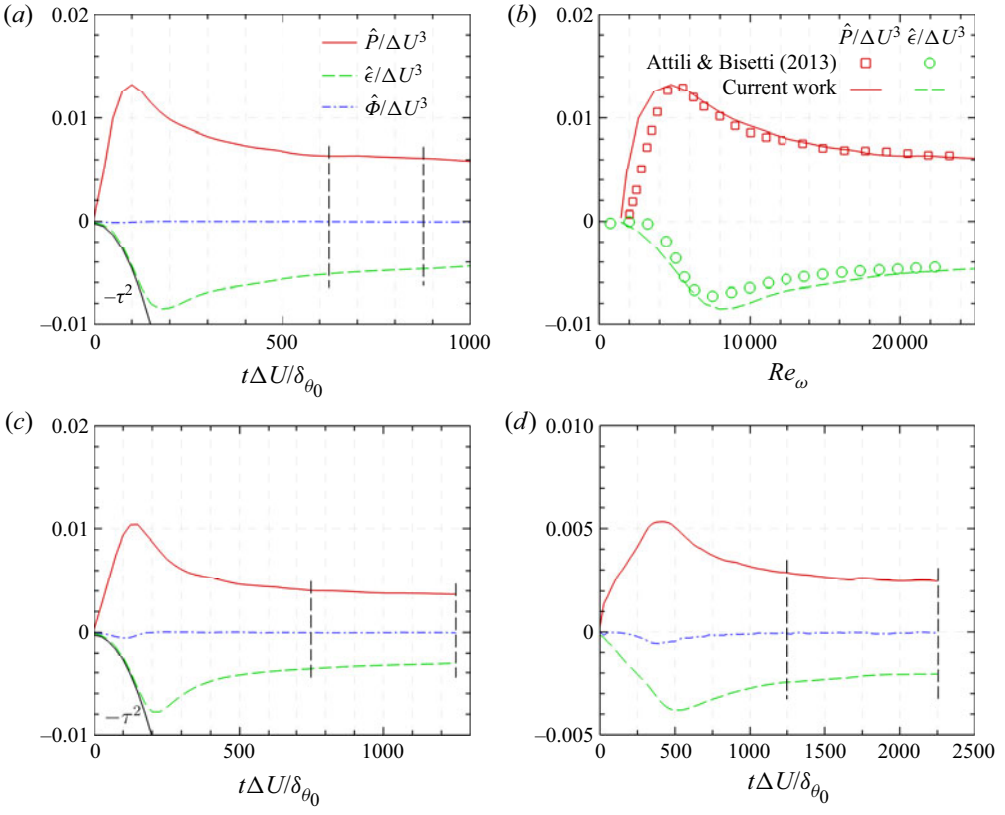


Figure 15. Time evolution of $\hat{P}/\Delta U^3$, $\hat{\epsilon}/\Delta U^3$, $\hat{\Phi}/\Delta U^3$ at (*a*),(*b*) $M_c = 0.2$, (*c*) $M_c = 0.8$ and (*d*) $M_c = 1.8$. The legend is the same for (*a*), (*c*) and (*d*). The black solid lines correspond to $\hat{\epsilon}/\Delta U^3 \propto -\tau^2$. The dashed vertical lines mark the self-similar time periods.

dissipation $\hat{\epsilon}$ in figure 15(*d*). We depict the PDF of three instantaneous viscous dissipation components $\epsilon_i/\Delta U^3$ at $\tau = 250$ in figure 17 for the convective Mach number $M_c = 0.2$ and 1.8, where $\epsilon_i$ is defined as (avoiding summation convention)

$$\epsilon_i = -\frac{1}{Re}\sigma'_{ik}\frac{\partial u''_i}{\partial x_k}. \tag{4.6}$$

The PDFs of $\epsilon_i/\Delta U^3$ always collapse into the same curve for $M_c = 0.2$. At convective Mach number $M_c = 1.8$, we observe that the left tail of PDF of $\epsilon_1/\Delta U^3$ is much longer than that of $\epsilon_2/\Delta U^3$ and $\epsilon_3/\Delta U^3$, suggesting that stronger events of viscous dissipation occur in the transport of $\hat{K}_1$ during the transition region. This is further studied from aspect of vortical structures in § 4.4.

We also plot the time evolution of transport terms for $\hat{R}_{12}$ in figure 18. For all cases, we can see that the transfer of the Reynolds shear stress is dominated by the pressure–strain term $\hat{\Phi}_{12}$ and production term $\hat{P}_{12}$ with peaks occurring at nearly the same time with the production $\hat{P}$. The viscous dissipation $\hat{\epsilon}_{12}$ is negligibly small and increases slightly as the convective Mach number increases.

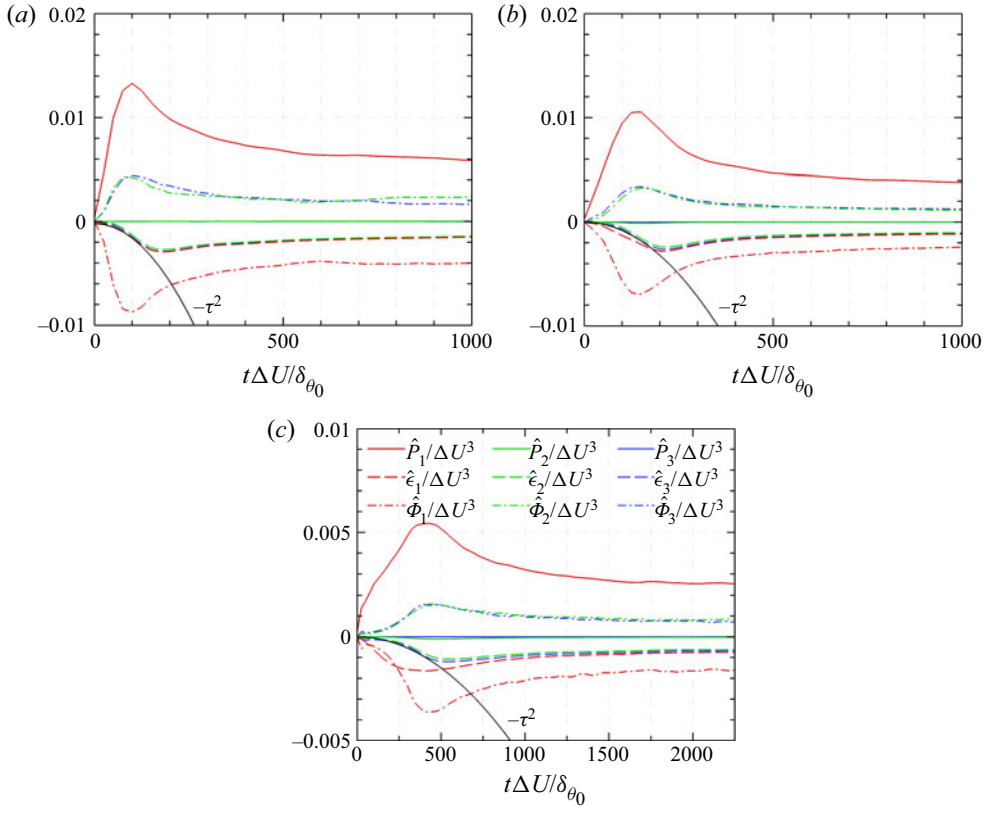


Figure 16. Time evolution of $\hat{P}_i/\Delta U^3$, $\hat{\epsilon}_i/\Delta U^3$, $\hat{\Phi}_i/\Delta U^3$ at (*a*) $M_c = 0.2$, (*b*) $M_c = 0.8$ and (*c*) $M_c = 1.8$. The legend is the same for all plots. The black solid lines correspond to $\hat{\epsilon}_i/\Delta U^3 \propto -\tau^2$.

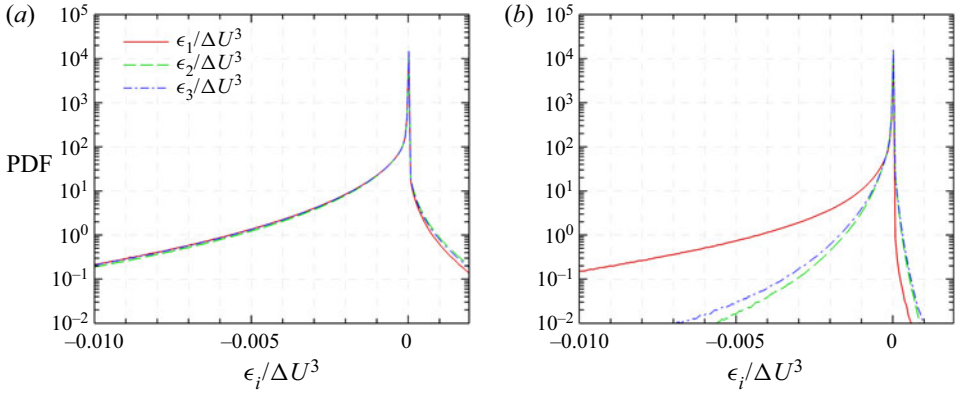


Figure 17. PDF of viscous dissipation components $\epsilon_i/\Delta U^3$ at $\tau = 250$ for cases with (*a*) $M_c = 0.2$ and (*b* $M_c = 1.8$.

### 4.4. *Turbulence structure and length scale*

As already mentioned, the contribution of dilatational component to overall Reynolds stress is quite limited. We therefore believe that the transportation of TKE is dominated by

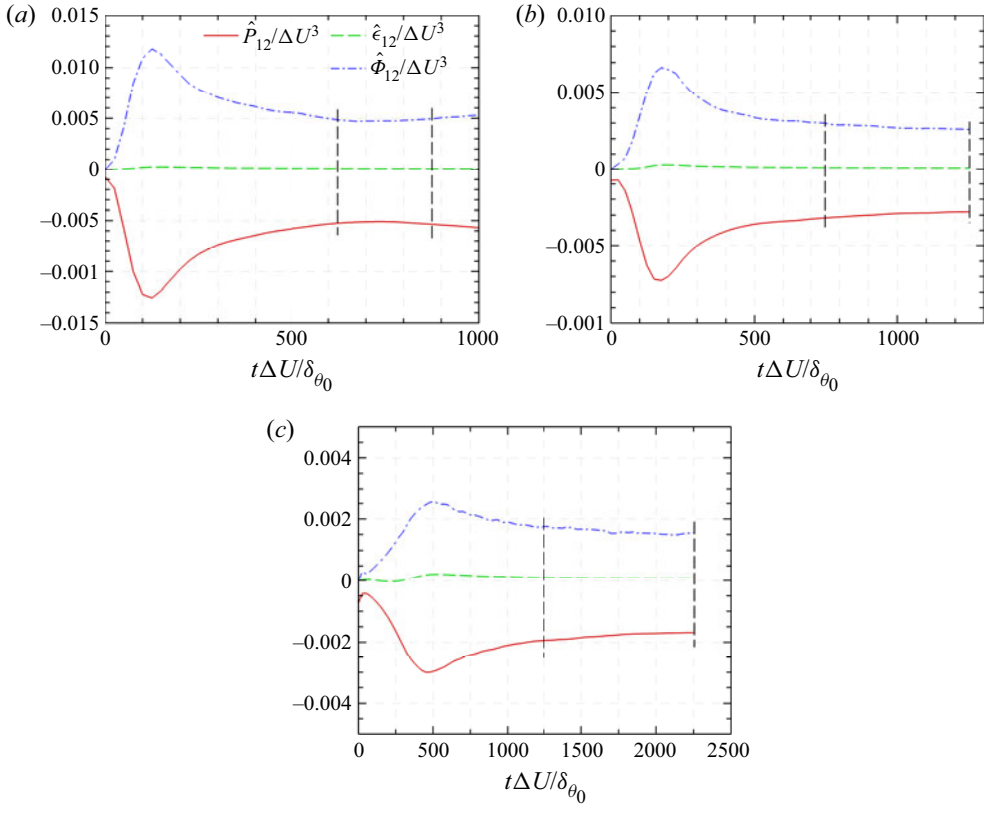


Figure 18. Time evolution of $\hat{P}_{12}/\Delta U^3$, $\hat{\epsilon}_{12}/\Delta U^3$, $\hat{\Phi}_{12}/\Delta U^3$ at (*a*) $M_c = 0.2$, (*b*) $M_c = 0.8$ and (*c*) $M_c = 1.8$. The legend is the same for all plots. The dashed vertical lines mark the self-similar time periods.

the solenoidal velocity field which is characterised by small-scale vortical structures and energetic large-scale velocity structures. According to Kolmogorov's turbulence theory (Kolmogorov 1941), the characteristic length scale of the smallest eddies is given by the Kolmogorov length scale $\eta$ where most of the kinetic energy is dissipated by viscosity. Figure 19(*a*) shows the temporal evolution of the normalised centreline Kolmogorov length scale $\eta_{y0}/\Delta x$ for cases with convective Mach numbers $M_c = 0.2$, 0.8 and 1.8. We observe that $\eta_{y0}/\Delta x$ at $y = 0$ reaches a minimum value during the transition region and then gradually increases as the development of turbulent flow. As the convective Mach number increases, the centreline Kolmogorov length scale $\eta_{y0}/\Delta x$ at $M_c = 1.8$ becomes twice as large as that at $M_c = 0.2$. From figure 19(*b*), it can be seen that the $\eta/\Delta x$ extracted in the self-similar region is approximately constant inside the turbulent mixing region, which is consistent with the previous results of compressible turbulent mixing layer by Vaghefi & Madnia (2015) and incompressible planar jet by Watanabe *et al.* (2018). Outside the mixing layer, $\eta/\Delta x$ decreases as the convective Mach number increases, due to the fluctuations induced by the shocklets here.

In figure 20, we compare the visualisations of small-scale vortical structures in transition region at $M_c = 0.2$ and 1.8, where the structures are displayed by the iso-surfaces of the second invariant of the instantaneous velocity gradient tensor $\boldsymbol{Q}$. At lower convective Mach number $M_c = 0.2$, the vortices are highly three-dimensional, with their diameter of the same order of the Kolmogorov scale. There are plentiful shapes of small-scale

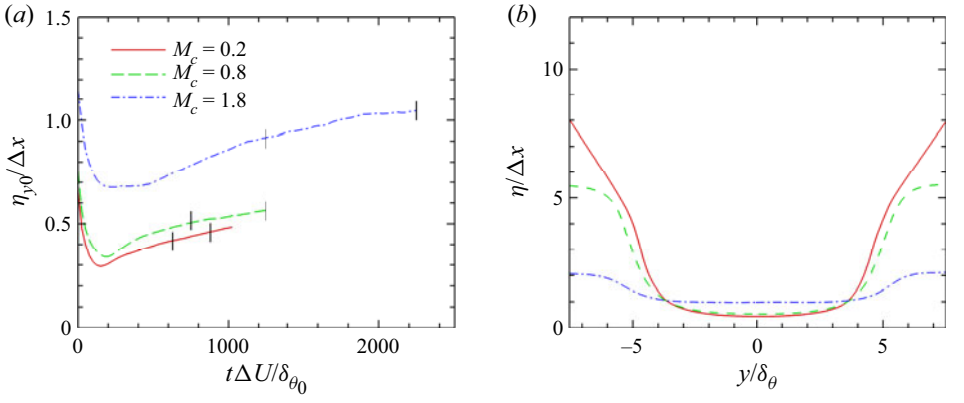


Figure 19. (*a*) Time evolution of the centreline Kolmogorov length scale $\eta_{y0}/\Delta x$ and (*b*) mean profile of $\eta/\Delta x$ at $M_c = 0.2$, 0.8 and 1.8. The dashed vertical lines mark the self-similar time periods in (*a*).

vortices, including hairpin vortices, rib vortices and complex helical vortices, giving rise to much random orientation of vortical structures. In contrast, the flow field is dominated by more regular and smooth streamwise elongated vortices at $M_c = 1.8$ and $\tau = 250$. This phenomenon is consistent with previous studies of small-scale vortical structures in compressible mixing layer, where it is generally believed that the vortical structures are more aligned in the streamwise direction at higher $M_c$, particularly in the transition region (Balaras *et al.* 2001; Fathali *et al.* 2008; Arun *et al.* 2019; Li *et al.* 2021).

The effects of the small-scale vortical structures on the anisotropy of viscous dissipation are further investigated by scrutinising flow variables in the $y$–$z$ planes, as shown in figure 21. In these $y$–$z$ slices at $x = 0.5L_x$, the black solid lines represent the iso-lines of viscous dissipation, whereas the contours show the velocity fluctuation. For case M02, the distribution of streamwise viscous dissipation $\epsilon_1$ is chaotic and fragmental, as shown in figure 21(*a*). Here $\epsilon_2$ and $\epsilon_3$ are not shown because they resemble $\epsilon_1$. For case M18, the mixing region is packed with mushroom-like structures of positive and negative streamwise velocity fluctuations, with strong streamwise viscous dissipation regions wrapping around them. Comparing figures 21(*b*) and 21(*c*), the lift-up of low-speed fluid and the drop-down of high-speed fluid are clearly presented. The prominent mushroom-like structures are created by the interaction of a pair of streamwise counter-rotating vortices, as presented in a enlarged view in figure 21(*e*), with the vectors showing the velocity fluctuations in the vertical $v''$ and spanwise $w''$ directions. This is similar to several previous studies on flat-plate boundary layers (Strand & Goldstein 2011; Buffat *et al.* 2014; Zhao & Sandberg 2020). From figures 21(*c*) and 21(*d*), we can see that the iso-lines of $\epsilon_2 = 0.005$ and $\epsilon_3 = 0.005$ are more sparse, with smaller length scales in the $y$–$z$ plane, as compared with the iso-lines of $\epsilon_1 = 0.01$, revealing that the viscous dissipation of $K_2$ and $K_3$ is much weaker than that of $K_1$ for $M_c = 1.8$ in the transition region, which confirms the results in figure 16.

We are now going to focus on the large-scale flow structures of the mixing shear layer. Figures 22 and 23 show the instantaneous fields of the streamwise velocity $u''$ and density fluctuations $\rho'$ in the horizontal plane at the centre of the shear layer ($y = 0$) at different time instants for cases M02 and M18, respectively. For the nearly incompressible case with $M_c = 0.2$, the density fields exhibit a typical pattern of spanwise Kelvin–Helmholtz rollers that merge and eventually fill up the whole computational domain, which is similar to the situation reported in incompressible (Rogers & Moser 1994; Balaras *et al.* 2001)

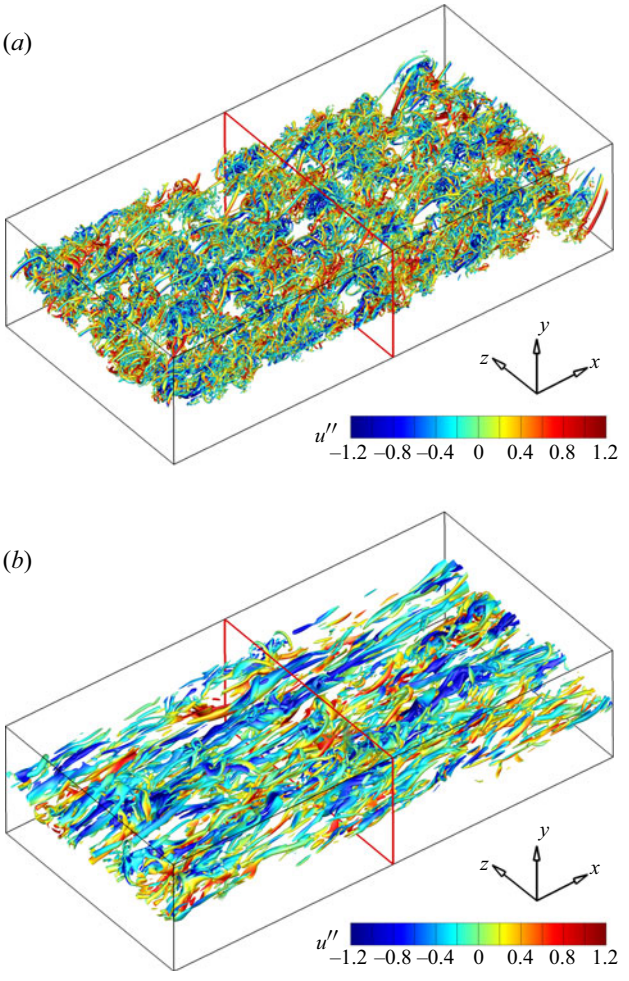


Figure 20. Small-scale vortical structures are visualised by the iso-surfaces of the second invariant $Q$ of the velocity gradient tensor and coloured based on local values of $u''$: (*a*) $Q = 20$, $\tau = 125$ and $M_c = 0.2$; (*b*) $Q = 2$, $\tau = 250$ and $M_c = 1.8$.

and weakly compressible (Mungal 1995; Pirozzoli *et al.* 2015) mixing shear layers. The streamwise elongated large-scale structures of $u''$ with an imposed low-frequency spanwise meander can also be observed in the transition region at $\tau = 375$. At late time $\tau = 750$, we can see that the high-speed regions tend to propagate abreast along the spanwise direction. For the strongly compressible case with $M_c = 1.8$, no clear hints of spanwise rollers can be observed both in the fields of the streamwise velocity $u''$ and density fluctuations $\rho'$. Although large-scale low- and high-speed regions form at an early time of $\tau = 125$, they are highly elongated in the streamwise direction and more slender in the spanwise direction.

To quantify the features of streamwise elongated large-scale structures in the mixing shear layer, the two-point correlation $R_{uu}$ (defined in (2.19)) at three different time instants in the self-similar region is shown in figure 24 at $M_c = 0.2$ and 1.8. Ten contour levels ranging from 0.1 to 1 with increments of 0.1 are shown and each direction is normalised by the local vorticity thickness $\delta_\omega$. The undulation of the lower $R_{uu}$ level is caused by the

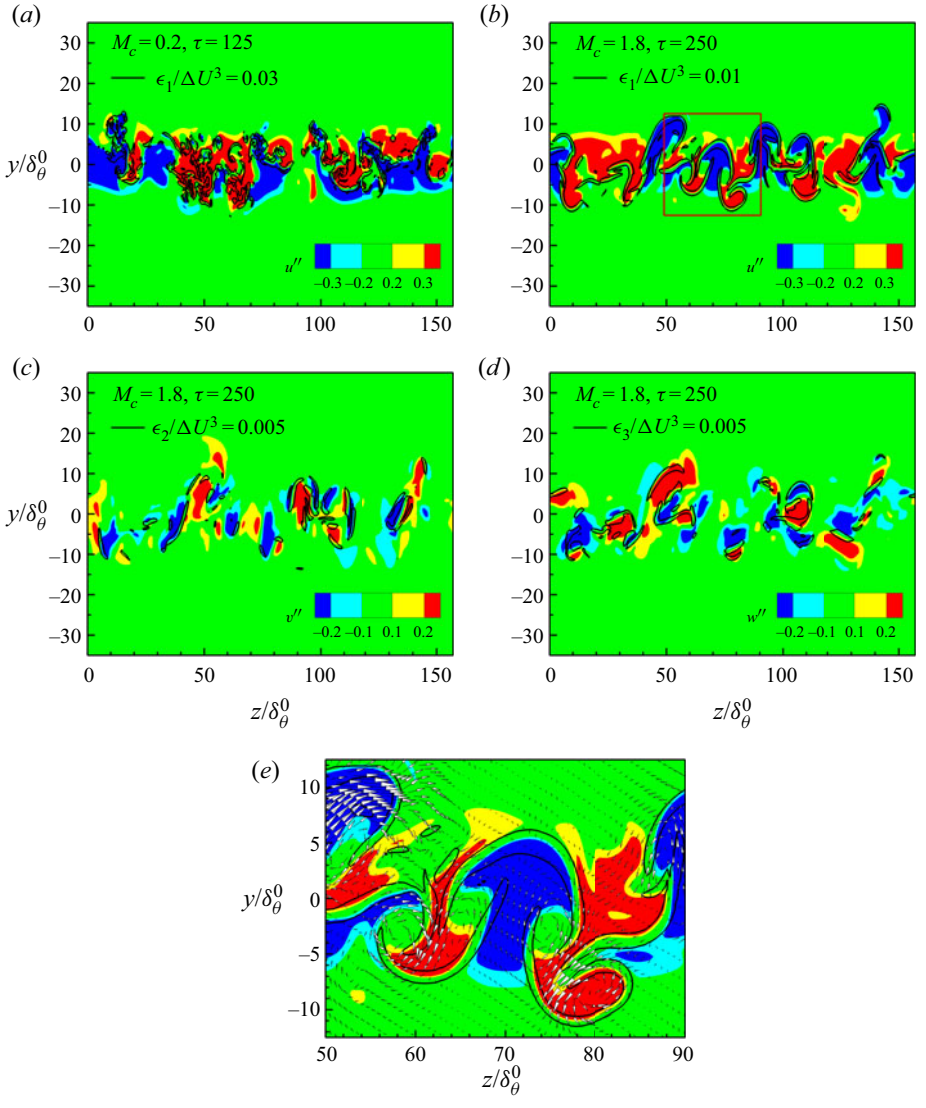


Figure 21. Contours of instantaneous velocity fluctuations $u_i''$ along with stronger events of viscous dissipation indicated by black solid lines: (*a*) $\epsilon_1/\Delta U^3 = 0.03$, $-0.3 < u'' < 0.3$ at $M_c = 0.2$ and $\tau = 125$; (*b*) $\epsilon_1/\Delta U^3 = 0.01$, $-0.3 < u'' < 0.3$, (*c*) $\epsilon_2/\Delta U^3 = 0.005$, $-0.2 < v'' < 0.2$, and (*d*) $\epsilon_3/\Delta U^3 = 0.005$, $-0.2 < w'' < 0.2$ at $M_c = 1.8$ and $\tau = 250$. (*e*) Enlarged view of the region in red-lined rectangular box in plot (*b*), showing the velocity vectors of $v$ and $w$.

decreasing sample size away from the origin. We find that the three sets of contours (at three different time instants) in the self-similar region show very good collapse when scaled by vorticity thickness $\delta_\omega$ for both $M_c = 0.2$ and 1.8, which confirms that the self-similar state of the mixing layer is dominated by large-scale structures (Vreman *et al.* 1996; Pantano & Sarkar 2002). In figures 24(*a*) and 24(*b*), the correlation decays to a value of 0.1 at a distance larger than $\delta_\omega$, which indicates that there is significant streamwise elongated spatial coherence. The fusiform-like correlation contours are inclined with respect to the local streamwise direction with an inclination angle decreasing from 18°

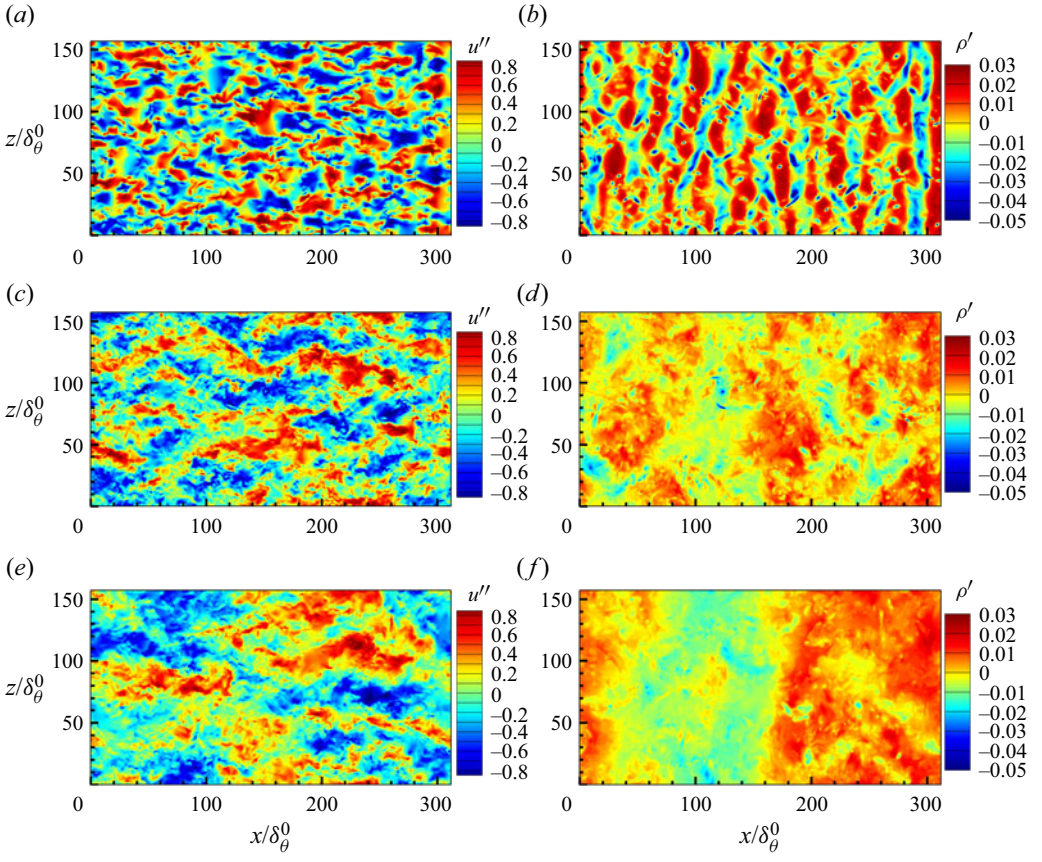


Figure 22. Instantaneous fields of (*a*),(*c*),(*e*) $u''$ and (*b*),(*d*),(*f*) $\rho'$ in the central $x$–$z$ plane for case M02: (*a*),(*b*) $\tau = 100$; (*c*),(*d*) $\tau = 375$; and (*e*),(*f*) $\tau = 750$.

at $M_c = 0.2$ to 12° at $M_c = 1.8$, which is similar to the experimental results reported by Messersmith & Dutton (1996) and Kim, Elliott & Dutton (2020). Figures 24(*c*),(*d*) and 24(*e*),(*f*) show $R_{uu}$ in the $x$–$z$ and $y$–$z$ planes, respectively. We find that the correlation contours are compact in spanwise direction and moderately elongated in the vertical direction, indicating a relatively small spanwise length scale.

In general, the streamwise and spanwise length scales of large-scale structures are extracted from the two-point correlation functions of the streamwise velocity fluctuations with a nominal threshold. A higher threshold leads to smaller and more stable coherence length (Ganapathisubramani *et al.* 2005; Sillero, Jiménez & Moser 2014). Here, it is found that the threshold strongly influences the streamwise correlation length, so it is difficult to determine the compressibility effect on the length scale. For example, when we chose a larger value of the threshold, $R_{uu} \geq 0.3$, the streamwise length scale was found to be larger at $M_c = 0.2$, in contrast to the situation of the threshold value 0.1. The compressibility effect on the length scale of large-scale structures is further investigated by inspecting the integral length scales, as shown in figure 25. We can see that the normalised integral length scales $l_x/\delta_\omega$ and $l_x/\delta_\omega$ rapidly decrease in the transition region from a very large initial value, then followed by a nearly constant length scale until the end of the simulation, confirming again the self-similarity of large-scale structures. This observation indicates that the current computational domain is large enough to solve the large-scale turbulence.

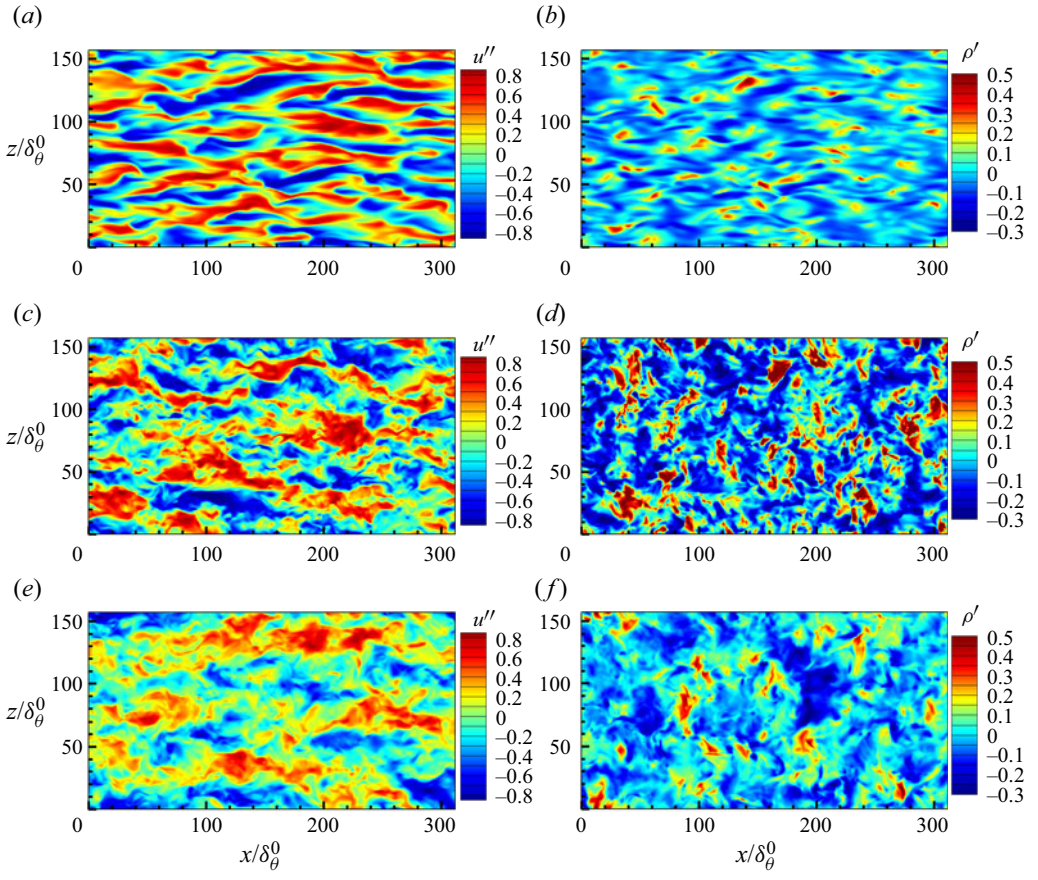


Figure 23. Instantaneous fields of $(a)$,$(c)$,$(e)$ $u''$ and $(b)$,$(d)$,$(f)$ $\rho'$ in the central $x$–$z$ plane for case M18: $(a)$,$(b)$ $\tau = 125$; $(c)$,$(d)$ $\tau = 500$; and $(e)$,$(f)$ $\tau = 2000$.

Otherwise, the growth of large-scale structures would be restricted resulting in the decrease of integral length scale (Vreman *et al.* 1996; Vadrot *et al.* 2021). In the self-similar region, the streamwise length scale $l_x/\delta_\omega$ increases significantly with the convective Mach number, indicating that the large-scale structures of $R_{uu}$ became increasingly elongated in the streamwise direction. As the convective Mach number increases, the spanwise integral length scale is almost unchanged with $l_z/\delta_\omega \approx 0.3$, whereas a clear decrease of the spanwise size of large scale structures can be found in figure 24. We also find that the spanwise integral length scale agrees very well with the previous study of a compressible spatially developing mixing layer (Pirozzoli *et al.* 2015).

In the stratified shear layer, the turbulent structures and flow dynamics have been found to resemble those in wall turbulence (Watanabe *et al.* 2019; Watanabe & Nagata 2021). The universality of the elongated large-scale structures can be examined in compressible temporally evolving mixing layers and turbulent boundary layers. The spanwise integral length scale is comparable to that observed in the logarithmic region of turbulent boundary layers (Pirozzoli & Bernardini 2011; Pirozzoli 2012), where $l_z/\delta \approx 0.2$–$0.3$ ($\delta$ is the thickness of the wall boundary layer). Figure 26 compares the two-point correlation of $u''$ in the present mixing shear layer with results reported in previous studies of the flat-plate boundary layers. We find that the two-point correlation at $M_c = 0.2$ is in excellent

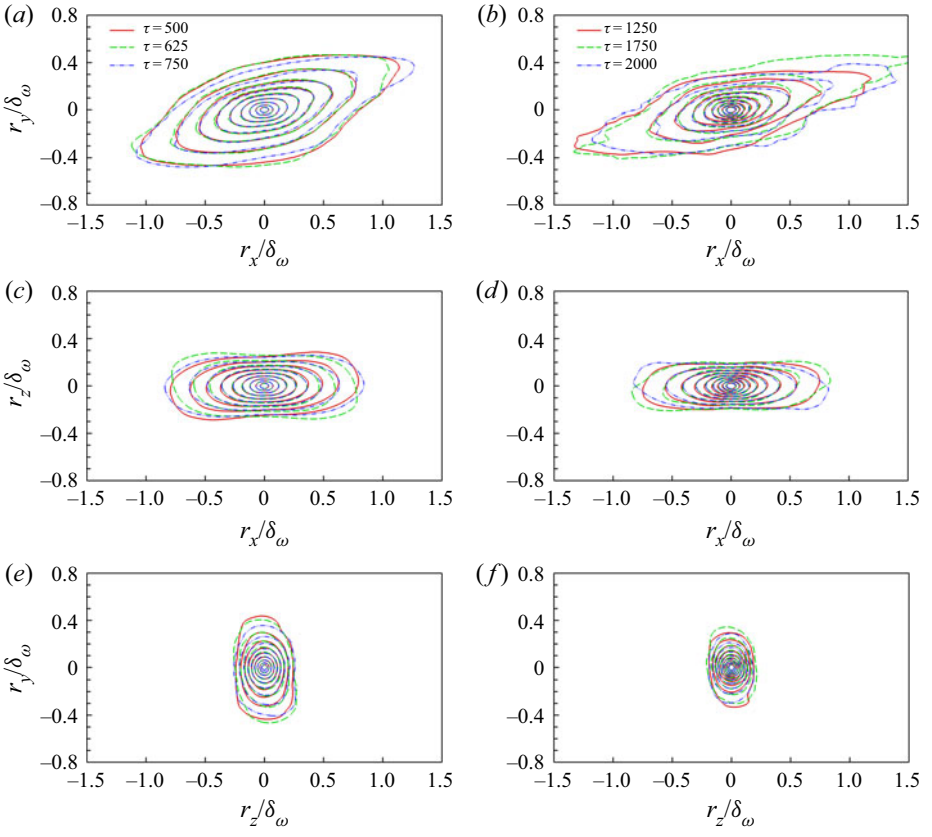


Figure 24. Two-point correlations of the streamwise velocity fluctuation $u''$ in the (*a*),(*b*) *x*–*y*, (*c*),(*d*) *x*–*z* and (*e*),(*f*) *y*–*z* planes at three different time instants: (*a*),(*c*),(*e*) $M_c = 0.2$ and (*b*),(*d*),(*f*) $M_c = 1.8$. The contour levels range from 0.1 to 1 with increments of 0.1.

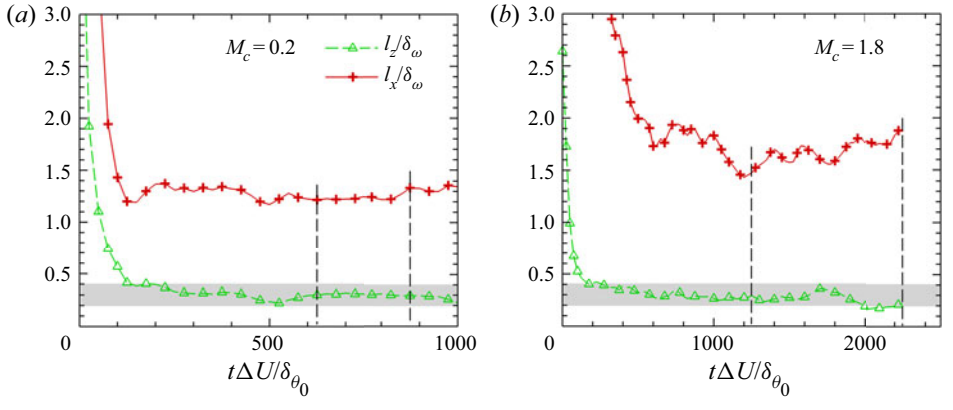


Figure 25. Evolutions of the normalised integral length scales in the streamwise direction $l_x/\delta_\omega$ and in the spanwise direction $l_z/\delta_\omega$ for (*a*) $M_c = 0.2$ and (*b*) $M_c = 1.8$. The dashed vertical lines mark the self-similar time periods.

agreement with the outer part of subsonic flat-plate boundary layers experimentally studied by Bross *et al.* (2021) with the centre of the contours located at $y/\delta = 0.2$. Near the wall (indicated by a red solid line), the contour line is stretched forming an extended

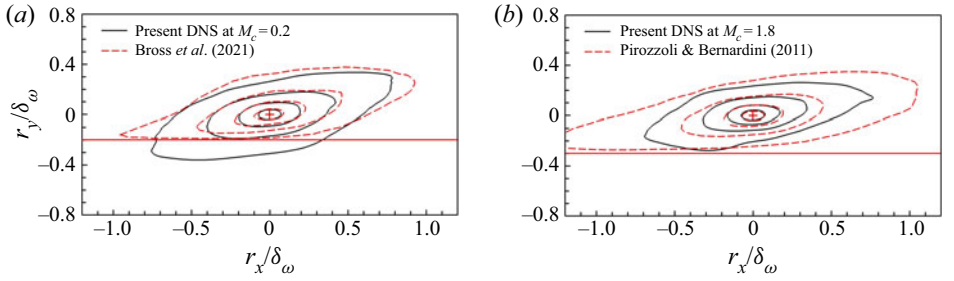


Figure 26. Comparisons of the two-point correlation of $u''$ in the mixing shear layer with that in the boundary layers (Pirozzoli & Bernardini 2011; Bross *et al.* 2021). The red solid lines indicate the wall of the boundary layer. The red + symbols show the centre points located with a distance of (*a*) $0.2\delta$ and (*b*) $0.3\delta$ away from the wall. The levels of contour lines are 0.2, 0.4, 0.6 and 0.8.

tail on the left side and compacted toward the centre of the structures. For the case with $M_c = 1.8$, the two-point correlation at lower level decays faster than that in supersonic flat-plate boundary layers measured by Pirozzoli & Bernardini (2011) with the centre of the contours located at $y/\delta = 0.3$, and the contour lines collapse well at high level of $R_{uu} \geq 0.6$. We infer that the disparity of the two-point correlation at $M_c = 1.8$ is caused by the arbitrary selection of the wall-normal location at which the correlation is computed in the boundary layer, due to the three-dimensional geometric properties of the large scale structures (Sillero *et al.* 2014; Kevin, Monty & Hutchins 2019*b*). As suggested by Kevin, Monty & Hutchins (2019*a*), the centre height $y/\delta = 0.2$ corresponds to the centre of the mean large-scale structures in the boundary layer, so we can expect a better comparison than that in figure 26(*b*).

In wall-bounded turbulence, the large-scale structures interact with the small-scale structures in two ways, namely the superposition and amplitude-modulation effects (Marusic *et al.* 2010; Mathis, Hutchins & Marusic 2011; Agostini & Leschziner 2014). A top view of high- and low-speed large-scale structures and small-scale vortical structures in the upper half-domain is given in figure 27 for $M_c = 1.8$. It is easy to identify two highly elongated low-speed (blue) regions flanked on either side in the spanwise direction by high-speed (red) regions, as shown in figure 27(*b*). Comparing figures 20(*b*) and 27(*a*), it is clear that the tendency of the vortical structures to align in the streamwise direction at high convective Mach number are much weaker at later times, which is consistent with the previous numerical analysis by Arun *et al.* (2019). We can see that the small-scale vortical structures have an apparent preference for clustering into the low-speed regions, and are more sparse in the high-speed regions. The iso-surface of low-speed regions acts as an envelope of the clustering small-scale structures. The observations are consistent with previous studies on wall turbulence (Marusic *et al.* 2010; Pirozzoli & Bernardini 2011; Chan & Chin 2022).

Moreover, we examined the conditionally averaged flow fields, $\langle u_i'' \mid u'' < 0\rangle$ and $\langle \omega \mid u'' < 0\rangle$, obtained by ensemble averaging $u_i''$ and $\omega$ around any point in the low-speed regions and at the centreplane $y = 0$, where $\omega$ is the vorticity magnitude. Figure 28 displays the conditionally averaged flow field in the $x$–$y$ and $y$–$z$ planes for $M_c = 0.2$ and 1.8. For both low and high convective Mach numbers, the large-scale low-speed structures are lifted upwards by a pair of counter-rotating quasi-streamwise vortices flanking the large-scale structures, as shown in figures 28(*b*) and 28(*d*), resembling the typical counter-rotating roll modes found in wall turbulence (Marusic *et al.* 2010; Kevin *et al.* 2019*a*). These quasi-streamwise roll modes in the mixing shear layer are inclined

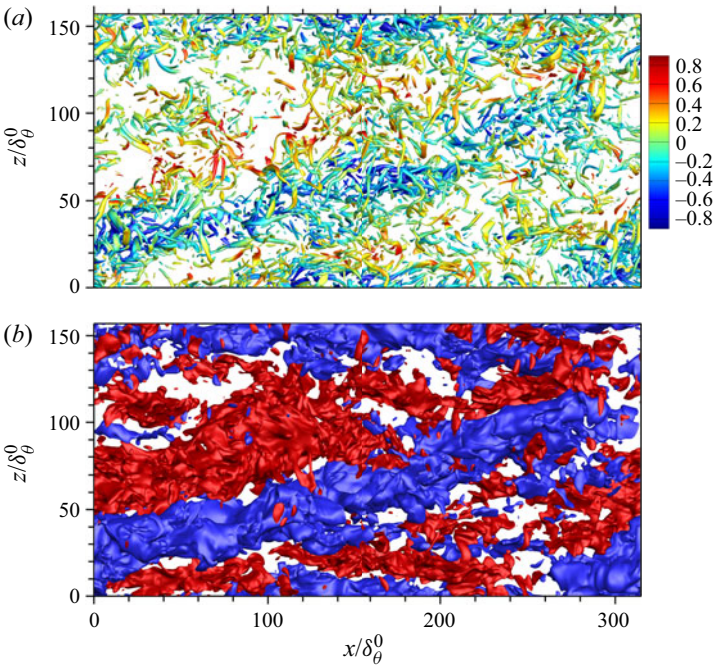


Figure 27. Top view of coherent structures in the upper half-domain $y > 0$ for $M_c = 1.8$ at $\tau = 1250$. (*a*) Small-scale vortical structures visualised by the iso-surfaces of the second invariant of the velocity gradient tensor $Q = 2$ and coloured based on local values of $u''$. (*b*) The high- and low-speed large-scale structures presented by the iso-surfaces of $u'' = 0.3$ (blue) and $-0.3$ (red), respectively.

slightly to the horizontal, which can be inferred from the orientation of velocity vectors in large-scale low-speed structures, as depicted in figures 28(*a*) and 28(*c*). The spanwise distance between two centres of the counter-rotating quasi-streamwise vortices clearly decreases as the convective Mach number increases, which is consistent with previous study of a compressible spatially developing mixing layer (Pirozzoli *et al.* 2015). At $M_c = 0.2$, we can see a clear sign of flow organisation into spanwise rollers located at both ends of conditionally averaged low-speed structures, which almost disappear at the highest convective Mach number $M_c = 1.8$, indicating that the effect of compressibility can suppress the Kelvin–Helmholtz instability.

Figure 28 also shows the distribution of the conditionally averaged vorticity intensity, $\langle \omega \mid u'' < 0 \rangle$. We find that, in the large-scale low-speed structures, the local maximum of $\langle \omega \mid u'' < 0 \rangle$ occurs at a higher distance from the centreline, confirming the clustering of small-scale vortical structures within the upper part of large-scale low-speed structures, as shown in figure 27. From figures 28(*a*) and 28(*c*), we can see that the clustering of small-scale vortical structures is directly associated with high-shearing motions presented by the longer arrow there. Taking into account the antisymmetry of the base flow $\tilde{u}_i(y) = -\tilde{u}_i(-y)$, the large-scale high- and low-speed structures statistically exhibit central symmetry patterns, therefore, the results on high-speed structures are not shown for brevity.

According to the present results, we propose a conceptual model for higher convective Mach number $M_c \geq 0.8$ to qualitatively depict the dynamics of the streamwise elongated large-scale structures and their interaction with small-scale vortical structures in the self-similar region, as illustrated in figure 29 viewed on a $y$–$z$ plane. This conceptual model

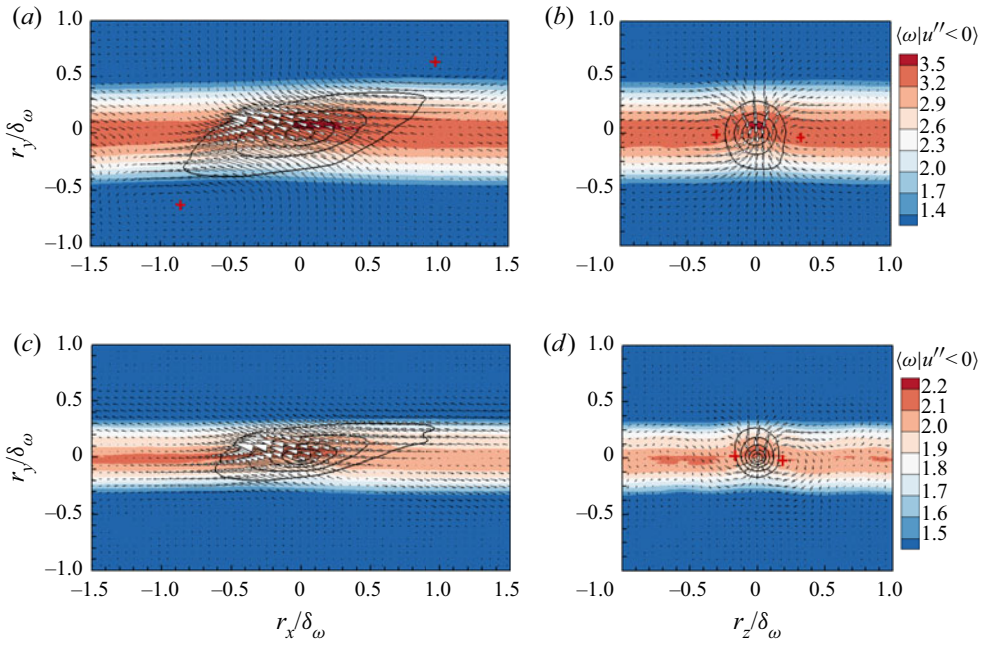


Figure 28. Conditional average of flow field conditioned to the low-speed structures, $u'' < 0$, in the (*a*),(*c*) $x$–$y$ and (*b*),(*d*) $y$–$z$ planes: (*a*),(*b*) $M_c = 0.2$ and (*c*),(*d*) $M_c = 1.8$. The colour contours display $\langle\omega \mid u'' < 0\rangle$ and $\langle u'' \mid u'' < 0\rangle$ is plotted with solid black contour lines representing levels range from $-0.2$ to $-0.05$ (from inside to outside) with increments of 0.05. Vectors represent conditional-averaged velocity components with the longest arrow measuring 0.2. The + (red) symbols show the centre location of roll modes.

resembles the outer part of the well-known model of wall-bounded turbulent flow proposed by Marusic *et al.* (2010). In this conceptual model, the high- (red) and the low-speed (blue) large-scale structures alternatively arrange in the spanwise direction with the associated counter-rotating roll modes (black circles) inducing the rising of the low-speed structures and the sinking of the high-speed structures. The embedding of the low-speed structures into the high-speed free stream results in a high-shear region promoting the small-scale vortical structures on top of the low-speed structures. Similarly, the small-scale vortical structures are activated at the bottom of high-speed large-scale structures. In the mixing layer, the large-scale high- and low-speed structures exhibit central symmetry about their symmetric centre on centreplane, whereas in the wall-bounded turbulence the near-wall part of the large-scale structures interact with the near-wall turbulence, through superposition and modulation effects (Mathis, Hutchins & Marusic 2009; Marusic *et al.* 2010; Mathis *et al.* 2011). It should be noted that, at low convective Mach number, the large-scale high- and low-speed structures and the spanwise rollers coexist, which deserves further study.

## 5. Conclusion

We have carried out the DNS of a temporal compressible shear layer to investigate the compressibility effects on statistical properties and coherent structures at the convective Mach numbers $M_c$ ranging from 0.2 to 1.8. The Reynolds number based on the momentum thickness and the free-stream velocity is initially set to 320 and becomes as large as 5200 in the self-similar region. We have given detailed comparisons of various flow statistics,

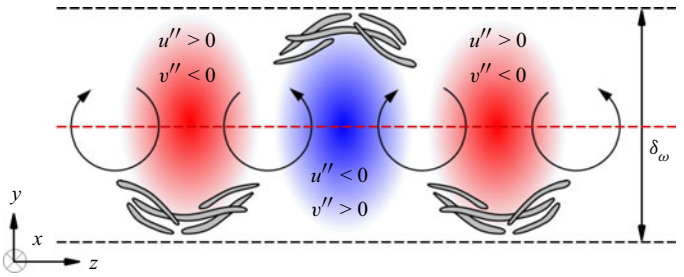


Figure 29. Schematic of large-scale coherent structures and its interaction across the mixing shear layer for higher convective Mach number $M_c \geq 0.8$. The red and blue regions indicate the high- and low-speed large-scale structures, respectively. The black circles is the counter-rotating roll modes. The gray contours show the clustering of small-scale vortical structures. The red and black dashed lines represent centreplane and boundaries of mixing layer, respectively.

including the mean velocity, momentum thickness, the Reynolds stresses and the balance of the TKE equation, with those in the previous experimental and numerical studies, and have validated our DNS data of a compressible mixing layer.

The local compressibility is investigated employing Helmholtz decomposition. As the convective Mach number increases, the magnitudes of three dilatation-related components of the Reynolds shear stress become larger, but still several orders of magnitude smaller than the solenoidal component. The physical mechanism of the suppression of layer growth rate due to compressibility is further examined by analysing the integrated statistics of the TKE budget. All integrated energy transfer terms undergo an overshoot in the transition region and approach an equilibrium state in the self-similar region. In the transition region, the vertical and spanwise components of viscous dissipation, $\hat{\epsilon}_2$ and $\hat{\epsilon}_3$, vary as approximately $-\tau^2$ at all convective Mach numbers. The streamwise component $\hat{\epsilon}_1$ varies like $-\tau^2$ at $M_c = 0.2$, and grows much faster than the other two components at $M_c = 1.8$ resulting in linear growth of the total dissipation. We found that the rapid increasing of $\hat{\epsilon}_1$ is strongly correlated with the streamwise elongated vortical structures at a higher level of compressibility. The lag of dissipation overshoot behind the production overshoot becomes smaller at higher convective Mach number $M_c = 1.8$. These observations indicate that the dissipation starts to effectively balance the production earlier at $M_c = 1.8$, revealing the compressibility effect on the reduction of growth rate.

Our numerical results confirm the existence of the large-scale high- and low-speed structures in the self-similar region, which accompany the spanwise Kelvin–Helmholtz rollers at low convective Mach number $M_c = 0.2$ and dominate the mixing layer solely at high convective Mach number $M_c = 1.8$. The two-point correlations of streamwise velocity fluctuation $u''$ are significantly elongated in the streamwise direction and compact in the spanwise direction, and are self-similar in the self-similar region. As the convective Mach number increases, the streamwise integral length scale $l_x/\delta_\omega$ increase significantly and the spanwise integral length scale $l_z/\delta_\omega$ is almost unchanged. The two-point correlations of $u''$ are in good agreement with those obtained in the logarithmic region of the compressible turbulent boundary layers. Moreover, in the conditionally averaged flow field, the large-scale low-speed structures are lifted upwards by a pair of counter-rotating quasi-streamwise rollers flanking the large-scale structures, resembling the typical counter-rotating roll modes found in wall turbulence. The spanwise Kelvin–Helmholtz rollers are located at both ends of the low-speed structures and strongly suppressed at the highest convective Mach number $M_c = 1.8$. The small-scale vortical structures have an apparent preference for clustering into the top of the low-speed regions,

| Case | $M_c$ | $L_x \times L_y \times L_z$ | $N_x \times N_y \times N_z$ | $L_b$ |
|---|---|---|---|---|
| G128 | 0.8 | $314 \times 314 \times 157$ | $256 \times 256 \times 128$ | 15.0 |
| G256 | 0.8 | $314 \times 314 \times 157$ | $512 \times 512 \times 256$ | 15.0 |
| G512 | 0.8 | $314 \times 314 \times 157$ | $1024 \times 1024 \times 512$ | 15.0 |
| B1 | 0.8 | $314 \times 314 \times 157$ | $1024 \times 1024 \times 512$ | 7.5 |
| B2 | 0.8 | $314 \times 314 \times 157$ | $1024 \times 1024 \times 512$ | 30.0 |

Table 2. Parameters for the additional simulations: $L_b$ denotes the buffer layer width; $L_x$, $L_y$, $L_z$ and $L_b$ are measured in terms of initial momentum thickness $\delta_\theta^0$.

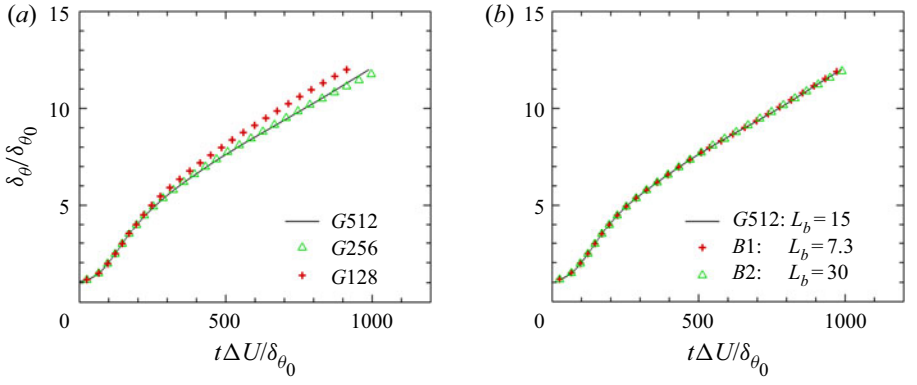


Figure 30. Temporal evolution of normalised momentum thickness at $M_c = 0.8$ for (*a*) different computational grid sizes and (*b*) different buffer layer width.

which is directly associated with high-shearing motions on top of the low-speed structures. These observations reveal the universality of the large-scale high- and low-speed structures in free shear and wall-bounded turbulent flows. Based on the present numerical results, the large-scale high- and low-speed structures are reconstructed by a conceptual model which resembles the outer part of the well-known model of wall-bounded turbulent flow proposed by Marusic *et al.* (2010).

**Funding.** This work was supported by the National Natural Science Foundation of China (NSFC Grants No. 91952104, No. 92052301, No. 12172161 and No. 12161141017), by the National Numerical Windtunnel Project (No. NNW2019ZT1-A04), by the NSFC Basic Science Center Program (Grant No. 11988102), by the Shenzhen Science and Technology Program (Grants No. KQTD20180411143441009), by Key Special Project for Introduced Talents Team of Southern Marine Science and Engineering Guangdong Laboratory (Guangzhou) (Grant No. GML2019ZD0103) and by Department of Science and Technology of Guangdong Province (Grants No. 2019B21203001). This work was also supported by Center for Computational Science and Engineering of Southern University of Science and Technology.

**Declaration of interests.** The authors report no conflict of interest.

**Author ORCIDs.**
Xiaoning Wang https://orcid.org/0000-0002-2616-6661;
Jianchun Wang https://orcid.org/0000-0001-5101-7791.

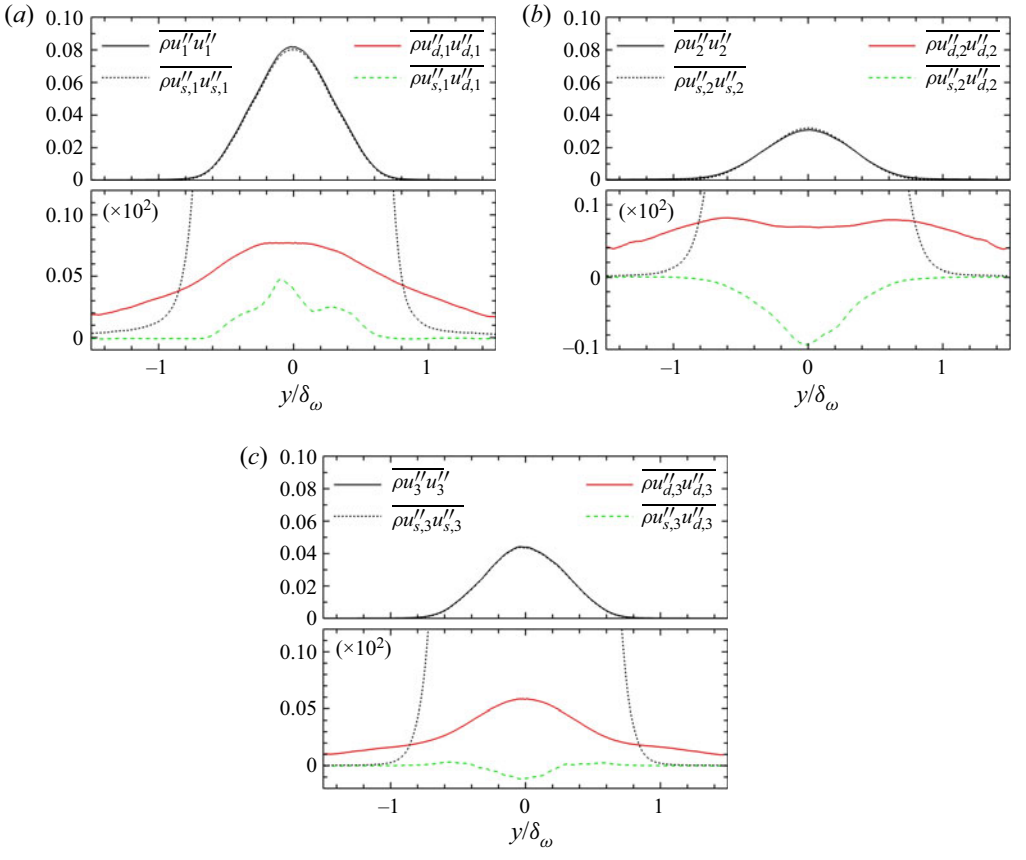


Figure 31. The Reynolds normal stresses and their decomposed components for case with $M_c = 1.8$: (*a*) $R_{11}$; (*b*) $\boldsymbol{R}_{22}$; and (*c*) $R_{33}$.

## Appendix A. Effect of resolution and buffer layer width

Several additional simulations have been performed at $Re_\theta = 320$ and $M_c = 0.8$ in order to explicitly investigate the effects of resolution and buffer layer width. The computational parameters corresponding to these simulations are summarised in table 2.

The grid resolution is examined on three sets of grids, namely, $256 \times 256 \times 128$, $512 \times 512 \times 256$ and $1024 \times 1024 \times 512$. The evolution of the normalised momentum thickness is shown in figure 30(*a*) for the three grid resolutions. It can be seen that clearly converged results are obtained for grids finer than $512 \times 512 \times 256$. Unless indicated otherwise, the results shown in the paper are based on the finest resolution $1024 \times 1024 \times 512$. Simulations B1 and B2 were performed with different buffer layer width $L_b = 7.5$ and 30.0, respectively, to ascertain the effect of buffer layer width. The turbulent field was initialised with the initial flow field of simulation G512 with $L_b = 15.0$. As shown in figure 30(*b*), the evolution of the normalised momentum thickness from three buffer layer widths overlap at all times, implying that the buffer layer width $L_b = 15.0$ is large enough to sufficiently damp disturbance at vertical boundary.

## Appendix B. Helmholtz decomposition of Reynolds normal stresses

In figure 31, we plot the Reynolds normal stresses and their decomposed components for cases with $M_c = 1.8$. Similar to $R_{12}$ in figure 13, the Reynolds normal stresses are

dominated by the solenoidal component in the turbulent region and by the dilatational component in the non-turbulent region. We find that $\overline{\rho u''_{d,2} u''_{d,2}}$ has two peaks at $y/\delta_\omega \approx \pm 0.6$, and $\overline{\rho u''_{d,1} u''_{d,1}}$ and $\overline{\rho u''_{d,3} u''_{d,3}}$ are single-peaked at $y = 0$. It is interesting to observe that the solenoidal-dilatational component $\overline{\rho u''_{s,1} u''_{d,1}}$ is positive, and $\overline{\rho u''_{s,2} u''_{d,2}}$ and $\overline{\rho u''_{s,3} u''_{d,3}}$ are negative in the turbulent region.

## References


Adrian, R.J. & Moin, P. 1988 Stochastic estimation of organized turbulent structure: homogeneous shear flow. *J. Fluid Mech.* **190**, 531–559.

Agostini, L. & Leschziner, M.A. 2014 On the influence of outer large-scale structures on near-wall turbulence in channel flow. *Phys. Fluids* **26** (7), 075107.

Arun, S., Sameen, A., Srinivasan, B. & Girimaji, S.S. 2019 Topology-based characterization of compressibility effects in mixing layers. *J. Fluid Mech.* **874**, 38–75.

Arun, S., Sameen, A., Srinivasan, B. & Girimaji, S.S. 2021 Scale-space energy density function transport equation for compressible inhomogeneous turbulent flows. *J. Fluid Mech.* **920**, A31.

Atoufi, A., Fathali, M. & Lessani, B. 2015 Compressibility effects and turbulent kinetic energy exchange in temporal mixing layers. *J. Turbul.* **16** (7), 676–703.

Attili, A. & Bisetti, F. 2012 Statistics and scaling of turbulence in a spatially developing mixing layer at $Re\,\lambda = 250$. *Phys. Fluids* **24** (3), 1–21.

Balaras, E., Piomelli, U. & Wallace, J.M. 2001 Self-similar states in turbulent mixing layers. *J. Fluid Mech.* **446**, 1–24.

Balsara, D.S. & Shu, C.W. 2000 Monotonicity preserving weighted essentially non-oscillatory schemes with increasingly high order of accuracy. *J. Comput. Phys.* **160** (2), 405–452.

Bell, J.H. & Mehta, R.D. 1990 Development of a two-stream mixing layer from tripped and untripped boundary layers. *AIAA J.* **28** (12), 2034–2042.

Birch, S.F. & Eggers, J.M. 1972 A critical review of the experimental data for developed free turbulent shear layers. *NASA Tech. Rep.* SP-321-vol 1, 11–40.

Bogdanoff, D.W. 1983 Compressibility effects in turbulent shear layers. *AIAA J.* **21** (6), 926–927.

Bross, M., Scharnowski, S. & Kähler, C.J. 2021 Large-scale coherent structures in compressible turbulent boundary layers. *J. Fluid Mech.* **911**, A2.

Brown, G.L. & Roshko, A. 1974 On density effects and large structure in turbulent mixing layers. *J. Fluid Mech.* **64** (4), 775–816.

Buchta, D.A. & Freund, J.B. 2017 The near-field pressure radiated by planar high-speed free-shear-flow turbulence. *J. Fluid Mech.* **832**, 383–408.

Buffat, M., Penven, L.L., Cadiou, A. & Montagnier, J. 2014 DNS of bypass transition in entrance channel flow induced by boundary layer interaction. *Eur. J. Mech.* B/*Fluids* **43**, 1–13.

Chan, C.I. & Chin, R.C. 2022 Investigation of the influence of miniature vortex generators on the large-scale motions of a turbulent boundary layer. *J. Fluid Mech.* **932**, A29.

Chen, S., Wang, J., Li, H., Wan, M. & Chen, S. 2018 Spectra and Mach number scaling in compressible homogeneous shear turbulence. *Phys. Fluids* **30** (6), 065109.

Chen, S., Wang, J., Li, H., Wan, M. & Chen, S. 2019 Effect of compressibility on small scale statistics in homogeneous shear turbulence. *Phys. Fluids* **31** (2), 025107.

Chinzei, N., Masuya, G., Komuro, T., Murakami, A. & Kudou, K. 1986 Spreading of two-stream supersonic turbulent mixing layers. *Phys. Fluids* **29** (5), 1345–1347.

Debisschop, J.R., Chambers, O. & Bonnet, J.P. 1994 Velocity field characteristics in supersonic mixing layers. *Exp. Therm. Fluid Sci.* **9** (2), 147–155.

Dimotakis, P.E. 1991 *Turbulent Free Shear Layer Mixing and Combustion*.

Erlebacher, G. & Sarkar, S. 1993 Statistical analysis of the rate of strain tensor in compressible homogeneous turbulence. *Phys. Fluids* A*: Fluid Dyn.* **5** (12), 3240–3254.

Fathali, M., Meyers, J., Rubio, G., Smirnov, S. & Baelmans, M. 2008 Sensitivity analysis of initial condition parameters on the transitional temporal turbulent mixing layer. *J. Turbul.* **9**, 1–28.

Foysi, H. & Sarkar, S. 2010 The compressible mixing layer: an LES study. *Theor. Comput. Fluid Dyn.* **24** (6), 565–588.

GANAPATHISUBRAMANI, B., HUTCHINS, N., HAMBLETON, W.T., LONGMIRE, E.K. & MARUSIC, I. 2005 Investigation of large-scale coherence in a turbulent boundary layer using two-point correlations. *J. Fluid Mech.* **524**, 57–80.

GOEBEL, S.G. & DUTTON, J.C. 1991 Experimental study of compressible turbulent mixing layers. *AIAA J.* **29** (4), 538–546.

GOTTLIEB, S. & SHU, C.-W. 1998 Total variation diminishing Runge–Kutta schemes. *Math. Comput.* **67** (221), 73–85.

HADJADJ, A., YEE, H.C. & SJÖGREEN, B. 2012 LES of temporally evolving mixing layers by an eighth-order filter scheme. *Intl J. Numer. Meth. Fluids* **70** (11), 1405–1427.

HICKEY, J.P., HUSSAIN, F. & WU, X. 2016 Compressibility effects on the structural evolution of transitional high-speed planar wakes. *J. Fluid Mech.* **796**, 5–39.

HUANG, P.G., COLEMAN, G.N. & BRADSHAW, P. 1995 Compressible turbulent channel flows: DNS results and modelling. *J. Fluid Mech.* **305**, 185–218.

JAHANBAKHSHI, R. & MADNIA, C.K. 2016 Entrainment in a compressible turbulent shear layer. *J. Fluid Mech.* **797** (2016), 564–603.

JIMÉNEZ, J. 2018 Coherent structures in wall-bounded turbulence. *J. Fluid Mech.* **842**, P1.

KEVIN, K., MONTY, J. & HUTCHINS, N. 2019*a* The meandering behaviour of large-scale structures in turbulent boundary layers. *J. Fluid Mech.* **865**, R1.

KEVIN, K., MONTY, J. & HUTCHINS, N. 2019*b* Turbulent structures in a statistically three-dimensional boundary layer. *J. Fluid Mech.* **859**, 543–565.

KIM, K.U., ELLIOTT, G.S. & DUTTON, J.C. 2020 Compressibility effects on large structures and entrainment length scales in mixing layers. *AIAA J.* **58** (12), 5168–5182.

KLEIN, M., SADIKI, A. & JANICKA, J. 2003 A digital filter based generation of inflow data for spatially developing direct numerical or large eddy simulations. *J. Comput. Phys.* **186** (2), 652–665.

KOLMOGOROV, A.N. 1941 The local structure of turbulence in incompressible viscous fluid for very large Reynolds numbers. *Dokl Akad Nauk SSSR* **30**, 299–303.

KOURTA, A. & SAUVAGE, R. 2002 Computation of supersonic mixing layers. *Phys. Fluids* **14** (11), 3790–3797.

KUMAR, G., BERTSCH, R.L. & GIRIMAJI, S.S. 2014 Stabilizing action of pressure in homogeneous compressible shear flows: effect of Mach number and perturbation obliqueness. *J. Fluid Mech.* **760** (1), 540–566.

LELE, S. 1989 Direct numerical simulation of compressible free shear flows. In *Center for Turbulence Research Annual Research Briefs*, pp. 79–98, Stanford University.

LELE, S. 1994 Compressibility effects on turbulence. *Annu. Rev. Fluid Mech.* **26** (1), 211–254.

LELE, S.K. 1992 Compact finite difference schemes with spectral-like resolution. *J. Comput. Phys.* **103** (1), 16–42.

LI, D., PEYVAN, A., GHIASI, Z., KOMPERDA, J. & MASHAYEK, F. 2021 Compressibility effects on energy exchange mechanisms in a spatially developing plane free shear layer. *J. Fluid Mech.* **910** (1), A9.

MA, Z. & XIAO, Z. 2016 Turbulent kinetic energy production and flow structures in compressible homogeneous shear flow. *Phys. Fluids* **28** (9), 096102.

MARUSIC, I., MATHIS, R. & HUTCHINS, N. 2010 Predictive model for wall-bounded turbulent flow. *Science (New York, NY)* **329** (5988), 193–196.

MATHIS, R., HUTCHINS, N. & MARUSIC, I. 2009 Large-scale amplitude modulation of the small-scale structures in turbulent boundary layers. *J. Fluid Mech.* **628**, 311–337.

MATHIS, R., HUTCHINS, N. & MARUSIC, I. 2011 A predictive inner–outer model for streamwise turbulence statistics in wall-bounded flows. *J. Fluid Mech.* **681**, 537–566.

MATSUNO, K. & LELE, S.K. 2021 Internal regulation in compressible turbulent shear layers. *J. Fluid Mech.* **907**, R2.

MESSERSMITH, N.L. & DUTTON, J.C. 1996 Characteristic features of large structures in compressible mixing layers. *AIAA J.* **34** (9), 1814–1821.

MUNGAL, M.G. 1995 Large-scale structure and entrainment in the supersonic mixing layer. *J. Fluid Mech.* **284**, 171–216.

PANTANO, C. & SARKAR, S. 2002 A study of compressibility effects in the high-speed turbulent shear layer using direct simulation. *J. Fluid Mech.* **451**, 329–371.

PAPAMOSCHOU, D. & ROSHKO, A. 1988 The compressible turbulent shear layer: an experimental study. *J. Fluid Mech.* **197** (1973), 453–477.

PIROZZOLI, S. 2012 On the size of the energy-containing eddies in the outer turbulent wall layer. *J. Fluid Mech.* **702**, 521–532.

PIROZZOLI, S. & BERNARDINI, M. 2011 Turbulence in supersonic boundary layers at moderate Reynolds number. *J. Fluid Mech.* **688**, 120–168.

PIROZZOLI, S., BERNARDINI, M., MARIÉ, S. & GRASSO, F. 2015 Early evolution of the compressible mixing layer issued from two turbulent streams. *J. Fluid Mech.* **777**, 196–218.

POPE, S.B. 2000 *Turbulent Flows*. Cambridge University Press.

RAGAB, S.A. & WU, J.L. 1989 Linear instabilities in two-dimensional compressible mixing layers. *Phys. Fluids* A **1** (6), 957–966.

ROGERS, M.M. & MOSER, R.D. 1994 Direct simulation of a self-similar turbulent mixing layer. *Phys. Fluids* **6** (2), 903–923.

ROSSMANN, T., MUNGAL, M.G. & HANSON, R.K. 2002 Evolution and growth of large-scale structures in high compressibility mixing layers. *J. Turbul.* **3**, 27–29.

SAMIMY, M. & ELLIOTT, G.S. 1990 Effects of compressibility on the characteristics of free shear layers. *AIAA J.* **28** (3), 439–445.

SAMTANEY, R., PULLIN, D.I. & KOSOVIĆ, B. 2001 Direct numerical simulation of decaying compressible turbulence and shocklet statistics. *Phys. Fluids* **13** (5), 1415–1430.

SANDHAM, N.D. & REYNOLDS, W.C. 1991 Three-dimensional simulations of large eddies in the compressible mixing layer. *J. Fluid Mech.* **224** (1991), 133–158.

SARKAR, S. 1995 The stabilizing effect of compressibility in turbulent shear flow. *J. Fluid Mech.* **282**, 163–186.

SHARAN, N., MATHEOU, G. & DIMOTAKIS, P.E. 2019 Turbulent shear-layer mixing: initial conditions, and direct-numerical and large-eddy simulations. *J. Fluid Mech.* **877**, 35–81.

SILLERO, J.A., JIMÉNEZ, J. & MOSER, R.D. 2014 Two-point statistics for turbulent boundary layers and channels at Reynolds numbers up to $\delta^+ = 2000$. *Phys. Fluids* **26** (10), 105109.

SMITS, A.J., MCKEON, B.J. & MARUSIC, I. 2011 High-Reynolds number wall turbulence. *Annu. Rev. Fluid Mech.* **43** (1), 353–375.

SPENCER, B.W. & JONES, B.G. 1971 Statistical investigation of pressure and velocity fields in the turbulent two-stream mixing layer. *AIAA Paper* 71-613.

STRAND, J.S. & GOLDSTEIN, D.B. 2011 Direct numerical simulations of riblets to constrain the growth of turbulent spots. *J. Fluid Mech.* **668**, 267–292.

SUTHERLAND, W. 1893 LII. The viscosity of gases and molecular force. *Lond. Edinb. Dublin Phil. Mag. J. Sci.* **36** (223), 507–531.

VADROT, A., GIAUQUE, A. & CORRE, C. 2020 Analysis of turbulence characteristics in a temporal dense gas compressible mixing layer using direct numerical simulation. *J. Fluid Mech.* **893**, A10.

VADROT, A., GIAUQUE, A. & CORRE, C. 2021 Direct numerical simulations of temporal compressible mixing layers in a Bethe–Zel'dovich–Thompson dense gas: influence of the convective Mach number. *J. Fluid Mech.* **922**, A5.

VAGHEFI, N.S. 2014 Simulation and modeling of compressible turbulent mixing layer. PhD thesis, Department of Mechanical and Aerospace Engineering, State University of New York at Buffalo.

VAGHEFI, N.S. & MADNIA, C.K. 2015 Local flow topology and velocity gradient invariants in compressible turbulent mixing layer. *J. Fluid Mech.* **774**, 67–94.

VAGHEFI, N.S., NIK, M.B., PISCIUNERI, P.H. & MADNIA, C.K. 2013 A priori assessment of the subgrid scale viscous/scalar dissipation closures in compressible turbulence. *J. Turbul.* **14** (9), 43–61.

VREMAN, A.W., SANDHAM, N.D. & LUO, K.H. 1996 Compressible mixing layer growth rate and turbulence characteristics. *J. Fluid Mech.* **320**, 235–258.

VREMAN, B., KUERTEN, H. & GEURTS, B. 1995 Shocks in direct numerical simulation of the confined three-dimensional mixing layer. *Phys. Fluids* **7** (9), 2105–2107.

WALLACE, J.M. 2016 Quadrant analysis in turbulence research: history and evolution. *Annu. Rev. Fluid Mech.* **48** (1), 131–158.

WANG, J., GOTOH, T. & WATANABE, T. 2017 Shocklet statistics in compressible isotropic turbulence. *Phys. Rev. Fluids* **2** (2), 1–19.

WANG, J., SHI, Y., WANG, L.-P., XIAO, Z., HE, X.T. & CHEN, S. 2012 Effect of compressibility on the small-scale structures in isotropic turbulence. *J. Fluid Mech.* **713**, 588–631.

WANG, J., WAN, M., CHEN, S. & CHEN, S. 2018 Kinetic energy transfer in compressible isotropic turbulence. *J. Fluid Mech.* **841**, 581–613.

WANG, J., WAN, M., CHEN, S., XIE, C., WANG, L.-P. & CHEN, S. 2019 Cascades of temperature and entropy fluctuations in compressible turbulence. *J. Fluid Mech.* **867**, 195–215.

WANG, J., WANG, L., XIAO, Z., SHI, Y. & CHEN, S. 2010 A hybrid numerical simulation of isotropic compressible turbulence. *J. Comput. Phys.* **229** (13), 5257–5279.

WANG, X., CHEN, S., WANG, J., LI, H., WAN, M. & CHEN, S. 2020 Effect of compressibility on the local flow topology in homogeneous shear turbulence. *Phys. Fluids* **32** (1), 015118.

WANG, X., WANG, J., LI, H. & CHEN, S. 2021 Kinetic energy transfer in compressible homogeneous anisotropic turbulence. *Phys. Rev. Fluids* **6** (6), 064601.

WANG, Y., TANAHASHI, M. & MIYAUCHI, T. 2007 Coherent fine scale eddies in turbulence transition of spatially-developing mixing layer. *Intl J. Heat Fluid Flow* **28** (6), 1280–1290.

WATANABE, T. & NAGATA, K. 2021 Large-scale characteristics of a stably stratified turbulent shear layer. *J. Fluid Mech.* **927**, A27.

WATANABE, T., RILEY, J.J., NAGATA, K., MATSUDA, K. & ONISHI, R. 2019 Hairpin vortices and highly elongated flow structures in a stably stratified shear layer. *J. Fluid Mech.* **878**, 37–61.

WATANABE, T., ZHANG, X. & NAGATA, K. 2018 Turbulent/non-turbulent interfaces detected in DNS of incompressible turbulent boundary layers. *Phys. Fluids* **30** (3), 035102.

XU, D., WANG, J., WAN, M., YU, C., LI, X. & CHEN, S. 2021*a* Compressibility effect in hypersonic boundary layer with isothermal wall condition. *Phys. Rev. Fluids* **6** (5), 054609.

XU, D., WANG, J., WAN, M., YU, C., LI, X. & CHEN, S. 2021*b* Effect of wall temperature on the kinetic energy transfer in a hypersonic turbulent boundary layer. *J. Fluid Mech.* **929**, 1–31.

YU, M., XU, C.X. & PIROZZOLI, S. 2019 Genuine compressibility effects in wall-bounded turbulence. *Phys. Rev. Fluids* **4** (12), 123402.

ZHAO, Y. & SANDBERG, R.D. 2020 Bypass transition in boundary layers subject to strong pressure gradient and curvature effects. *J. Fluid Mech.* **888**, A4.

ZHOU, Q., HE, F. & SHEN, M.Y. 2012 Direct numerical simulation of a spatially developing compressible plane mixing layer: flow structures and mean flow properties. *J. Fluid Mech.* **711**, 437–468.